BOEING SCIENTIFIC RESEARCH LABORATORIES DOCUMENT D1-82-05

BOEING

SCIENTIFIC RESEARCH LABORATORIE

Stress Corrosion Cracking of Titanium Alloys Preliminary Report on Ti:8Al-1Mo-1V Alloy and Proposed Electrochemical Mechanism

T. R. Beck

SOLID STATE PHYSICS LABORATORY JULY 1965

D1-82-0554

STRESS CORROSION CRACKING OF TITANIUM ALLOYS
PRELIMINARY REPORT ON Ti:8Al-1Mo-1V ALLOY
AND PROPOSED ELECTROCHEMICAL MECHANISM

by

T. R. Beck

July, 1966

Solid State Physics Laboratory

Boeing Scientific Research Laboratories

Seattle, Washington 98124

TABLE OF CONTENTS

SUMMARY

Stress corrosion cracking of titanium: 8% Al - 1% Mo - 1% V alloy specimens was investigated in various salt solutions at controlled potentials applied by a potentiostat. Polarization curves on titanium oxide surfaces and kinetic data for oxidation of newly formed titanium alloy surface were also obtained.

It was found that stress corrosion cracking of duplex annealed Ti:8-1-1 alloy occurred in chloride, bromide, and iodide solutions but did not occur in other solutions such as fluoride, hydroxide, sulfide, sulfate, nitrate or perchlorate. The ultimate strength was strongly dependent upon potential. The velocity of crack propagation and current flowing into the crack in chloride, bromide and iodide solutions were linearly related to the applied potential above a potential of -900 mv to the saturated colomel electrode.

An electrochemical model was developed to interpret the data. Anodic reaction with the halides is considered to initiate at the -900 mv potential and the rate of crack propagation to be limited by the potential drop through the electrolyte in the crack. It is planned to extend the investigation to other alloys using the model as a guide for the design of experiments.

INTRODUCTION

The first known report on stress corrosion cracking (SCC) of titanium dates back to Kiefer and Harple, 1953, who described cracking phenomena with commercially pure titanium in red fuming nitric acid. This finding apparently did not stimulate much farther work because red fuming nitric acid is rather an unusual environment.

"Hot salt cracking" of titanium alloys was discovered in the mid 1950's in connection with creep in turbine blades. The subject became very active in the early 1960's because of the impact of SCC on the supersonic transport program. A considerable amount of sponsored research has been conducted on this topic, some of which was reported at the Pacific Area National Meeting of the ASTM in Seattle in November 1965.

The first known report of stress corrosion cracking of titanium alloys in room temperature aqueous environments was that of Brown, 1965. He found that precracked specimens of titanium: 8% aluminum - 1% molybdenum - 1% vanadium alloy (Ti:8-1-1) were susceptible to SCC in sea water. This touched off a new flurry of investigation in the aerospace industry for suitable less-susceptible alloys for the supersonic transport. Although much applied work was done and less-susceptible alloys were found, the mechanism of SCC in titanium alloys was still unknown.

In order to establish a firmer basis for understanding SCC of titanium alloys within the Boeing Company, basic research was initiated at the Boeing Scientific Research Laboratories (BSRL) in

mid 1965. Experimental work began in September when experimental apparatus became available. This interim report summarizes experimental results and theoretical development at BSRL from September 1965 through May 1966.

At the start of the program four mechanisms were proposed as the most probable for the stress corrosion cracking of titanium alloys (Beck and Blackburn, 1965):

1. A mechanism involving hydrogen.
   a) Stepwise formation and fracture of brittle surface hydride layer at the apex of a crack.
   b) Precipitation of a hydride phase within the plastic zone due to a more rapid diffusion and/or easier nucleation, leading to a degradation of properties in this region.
2. A mechanism involving titanium dioxide.
   a) Stepwise formation and fracture of brittle titanium dioxide layer at the apex of a crack.
   b) Wedging of a crack by formation of titanium dioxide.
3. Preferential anodic dissolution at specific electrochemically active sites at the apex of a crack.
4. A mechanism involving adsorption of a species from the electrolyte phase in contact with the metal.
   a) Lowering of surface energy and cleavage as envisaged in the Griffith fracture mechanism.
   b) Interaction with generation or movement of dislocations in plastic zone at the apex of a crack.

All four models had the common feature that they were sensitive to the electrical potential of the metal surface in aqueous solution, although in different ways. Application of controlled potential was therefore believed to be a powerful tool in distinguishing between the various models.

The following items of work were outlined by Beck and Blackburn, 1965, as a means to determining the SCC mechanism of titanium alloys:

1) Determine electrochemical polarization curves for a variety of alloys and heat treatments and electrolyte compositions.

2) Conduct tensile tests with notched specimens of a variety of titanium alloys and heat treatments in electrolyte environments at controlled potentials based on 1).

3) Conduct a limited number of engineering tensile tests on standard precracked specimens of selected alloys and heat treatments at selected electrolyte environment compositions and potentials based on 2).

4) Conduct applicable physical, metallurgical, and chemical examinations including determination of fracture path.

5) Conduct theoretical analysis of mechanisms in conjunction with 1) through 4).

The work reported to date includes determination of polarization curves and tensile strength of Ti:8-1-1 in a range of electrolyte environments and potentials, and development of a theoretical model which fits the experimental facts to date. The purpose of the theoretical model was to help in designing definitive experiments.

The model is semiquantitative at this point in time and further work is planned as described herein.

A table of nomenclature used in this report and some supplementary data are given in the Appendices. Complete data for all of the experiments run to date are in the process of tabulation on punched cards for further correlation and are available at BSRL. All potentials recorded in the experiments are given in millivolts in this report. Unless otherwise stated, the saturated colomel electrode (SCE) is the zero standard of reference.

EXPERIMENTAL

Titanium: 8-1-1 was chosen as the alloy for initiating the program because it had been shown by prior investigators to be one of tne titanium alloys most susceptible to SCC. It was available from the supplier, Titanium Metals Corporation, in two heat treatments; mill annealed and duplex annealed. The mill annealed treatment consisted of holding the sheet at 788°C for 8 hours, followed by furnace cooling. The duplex annealed treatment consisted of re-heating mill annealed sheet to 788°C for 15 minutes followed by air cooling. The compositon and tensile properties of the material used in this investigation are given in Table I.

Table I

Composition and Tensile Properties of

Metal used in this Investigation

	Commercially Pure Foil[1]	Duplex Annealed[2]	Duplex Annealed[3]	Mill Annealed[4]
Thickness - in.	0.0015	0.050	0.060	0.060
Sheet No.	-	2936	2194	2026
Heat Treat No.	M8020	B9093-F-2284	3960831	D2654
Composition - %				
Al	-	8.0	7.6	7.55
Mo	-	1.00	1.05	1.05
V	-	1.01	0.98	0.95
Fe	0.05	0.04	0.11	0.16
C	0.014	0.03	0.04	0.045
N	0.009	0.0045	0.0008	0.001
H	0.007	0.0069	0.0042	0.005
O	N.A.	0.075	0.109	0.047
Yield Strength KSI	86.5	129.2 129.5	137.8 137.5 137.6	148.0 148.7 149.8
UTS - KSI	95.5	141.6 141.4	145.8 144.9 144.9	156.2 156.9 158.7
Elong. - %	30	10.5 10.5	11.5 12.0 10.5	13.0 13.0 13.0

Notes:

1. Data from Titanium Metals Corp. Foil used in polarization experiments.
2. Data from Boeing Airplane Division. This sheet used for most of the tensile experiments reported herein.
3. Data from Boeing Airplane Division. Few tensile tests on this sheet.
4. Data from Boeing Airplane Division. This sheet used for oxidation kinetics experiments.

A. Polarization Curves

The potentiostatic technique was used for determining polarization curves for titanium. The experimental setup is shown in Fig. 1.

The cell was a 150 ml Pyrex beaker with a Plexiglas cover. The titanium working electrode was generally a strip of thin sheet or foil about 1/8 inch wide and with about 1/2 inch immersion in the electrolyte. A platinum counter electrode was used. The reference electrode was a Beckman fiber-junction saturated calomel type. It was placed in a tube containing the electrolyte under study. This tube had a second fiber junction within the Luggin capillary tip which was placed next to the working electrode. This arrangement avoided KCl contamination of the electrolyte under study in the cell.

The potential was either changed stepwise by adjusting the reference voltage in the Wenking potentiostat or changed linearly with time. The linear sweep device was fabricated using a motor driven Helipot connected across a 5.2 volt mercury battery.

A pair of 1N250 diodes was used as a linear-to-logarithmic converter for the current. This arrangement allowed plotting both anodic and cathodic current without switching. The diodes were linear in the logarithm over about four decades, and did not change measurably with age. A typical calibration curve is shown in Fig. 2. The temperature coefficient of potential is about -3 mv per degree Centigrade for a given current.

The polarization curves were made for the purpose of scanning

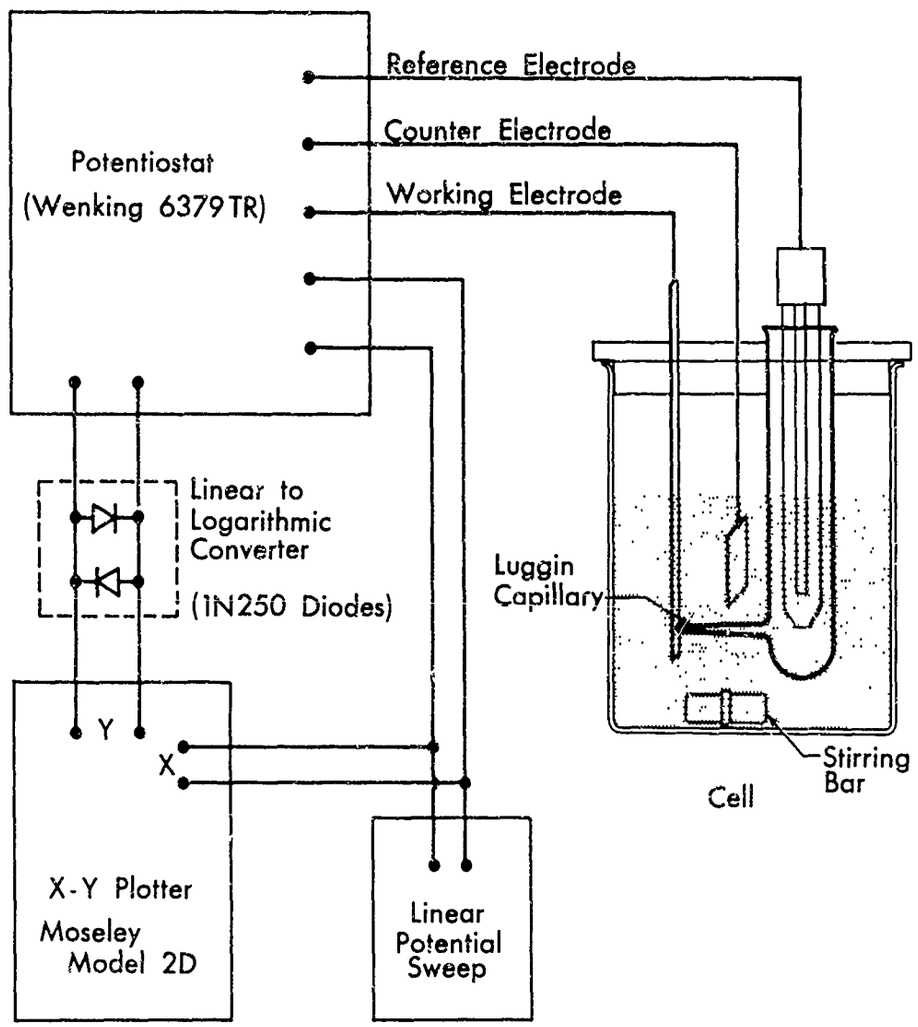

Fig. 1 Experimental setup for determining polarization curves.

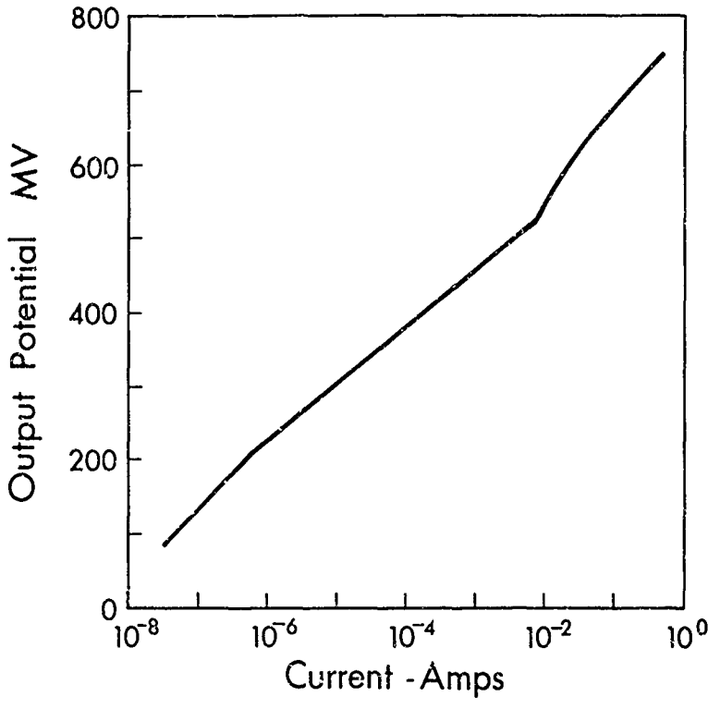

Fig. 2 Calibration of 1N250 diode linear-to-logarithmic signal converter.

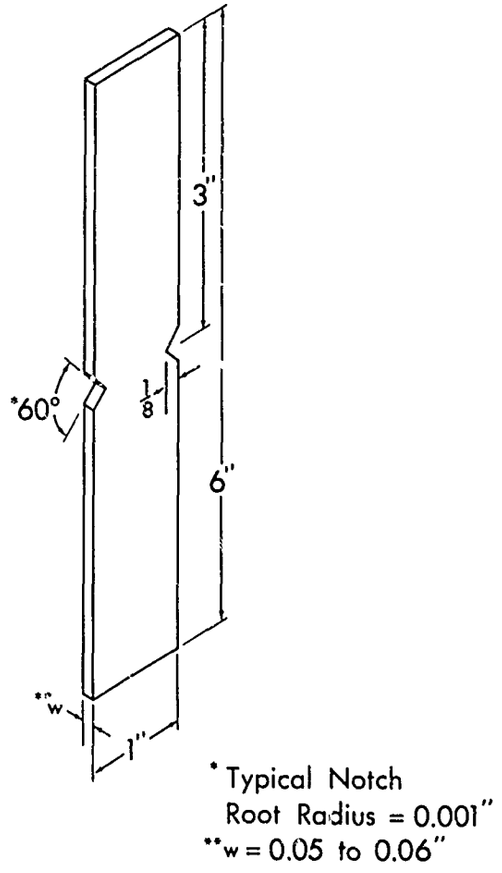

Fig. 3 Tensile specimen geometry.

for gross effects and are subject to a number of limitations in examining fine detail. The limitations are:

1. The cell and diodes were not thermostated. Air conditioned room temperature in the laboratory varied from 67 to 72°F.
2. Anode and cathode were in the same compartment, resulting sometimes in cross-contamination of products, e.g., chlorine produced at counter electrode could be reduced at the working electrode.
3. Saturation of electrolyte by air led to oxygen reduction under certain conditions.
4. Shape of electrodes and geometry of placement gave non-uniform current density distribution at high current density.
5. Ohmic drop existed between Luggin capillary and working electrode at high current density.
6. Mass transport limiting processes were not under control. Qualitatively, the presence of mass transport limitation could be observed by stirring.
7. Some of the solutions tested were stored in polyethylene bottles which could have contributed some contamination.

B. Tensile Tests

Tensile tests were performed with notched specimens in a 10 Kg Instron Model TT universal testing instrument. The specimens were gripped in Instron G-61-10F Type 10F wedge action jaws.

The tensile specimen geometry is shown in Fig. 3. The criteria

for selection of the specimen geometry were:

1. The specimens should be such a size and shape that stress corrosion cracking could be produced.
2. The specimens should fit the jaws and capacity of the tensile machine.
3. The specimens should be inexpensive and easy to produce and use so that hundreds could be used to screen environmental effects.

It was also considered desirable that the specimens should be designed according to fracture mechanics concepts but this was not compatible with the above criteria. It is intended to follow up later with larger size specimens designed according to fracture mechanics concepts.

The specimens were prepared by shearing from sheet stock slightly oversize blanks and the two long edges were machined to finished dimensions. The first specimens were double notched but later specimens were single notched. Tolerance on the net section width was held to ±0.002 inch. The cutter was resharpened between the final passes during cutting of the notches in order to minimize cold working and to obtain a more precise notch root radius. Most specimens had a notch root radius of 0.001 inch. Cutting oil was subsequently removed from the specimens by a kerosene followed by an acetone rinse. The later samples were anodized to 70-80 volts in a 1 normal sulfuric acid bath to minimize electrolytic reactions on the surface during the tensile tests. The specimens were not precracked. In the tensile tests, a crosshead velocity of 0.005 cm/minute was selected as standard

for most of the tests. This selection was made after a preliminary screening to determine effect of crosshead speed on specimen strength as described under results. The specimens were usually preloaded in the elastic region to about 1000 Kg (2200 lbs) at a crosshead velocity of 0.05 to 0.10 cm/minute. This procedure permitted tests to be completed in a period of 10 to 30 minutes. Rapid testing was considered necessary in order to evaluate a wide range of environments. Force-time plots were recorded in each test.

Tests were made in air and in various electrolyte solutions, with the specimen potentiostatically held at a preset potential. Electrically the setup shown in Fig. 1 was used, but with constant reference potential rather than programmed linear potential change. Electrical connection to the specimens was made through the wedge action jaws. Current flowing to the specimen was recorded versus time during the test using an x-axis speed of 1/50 in/sec on the x-y plotter. The Teflon cell configuration used in the later tests is illustrated in Fig. 4. A polyethylene cup cemented to the specimens with RTV silicone rubber cement was used for earlier tests.

The first tests were made with 3½ percent sodium chloride (0.6 molar) solution, corresponding to the total salt content of seawater. Other salt solutions for comparison were also made 0.6 molar. Concentration effects were studied later.

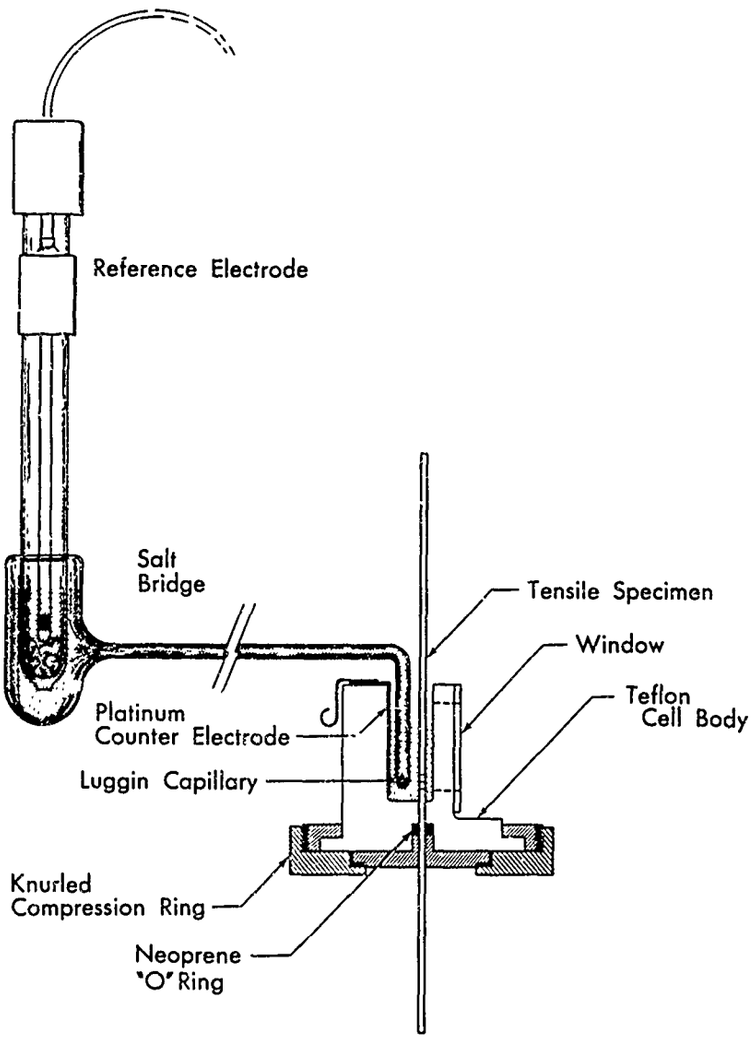

Fig. 4 Configuration of cell for tensile specimens.

C. Kinetics of Oxidation

During the testing it was observed that mill annealed Ti:8-1-1 alloy was extremely brittle and failed extremely rapidly by cleavage, even in air. This provided an opportunity to measure electrochemically the kinetics of oxidation of freshly generated metal surface. These data were used to interpret the mechanisms occurring during stress corrosion cracking.

Experimentally the procedure was similar to that used in the tensile tests except that a higher crosshead velocity (0.5 cm/minute) was used. Current was recorded on the x-y plotter using a x-axis speed of 2 inch/sec at fracture. The oxidation current to the new surface is that current measured after final failure (see Fig. 15) corrected for current to the old exterior surface. The x-axis speed was subsequently reduced during the test in order to get the longer term current transient. The specimens were usually anodized to minimize the correction for background current to the old surface exterior to the crack. Where the background current was significant, a correction was made to the measurement to get current to the new surface.

In later experiments a Tektronix type 545 A oscilloscope and Polaroid camera were used to record the current transient at less than 10^{-1} second from final fracture. For the most recent experiments a special cell illustrated in Fig. 5 was designed for studying oxidation kinetics. Size of the specimen was minimized to keep the current within the limits of the potentiostat and to minimize capacitive errors. The Luggin capillary-to-specimen spacing was more rigidly controlled

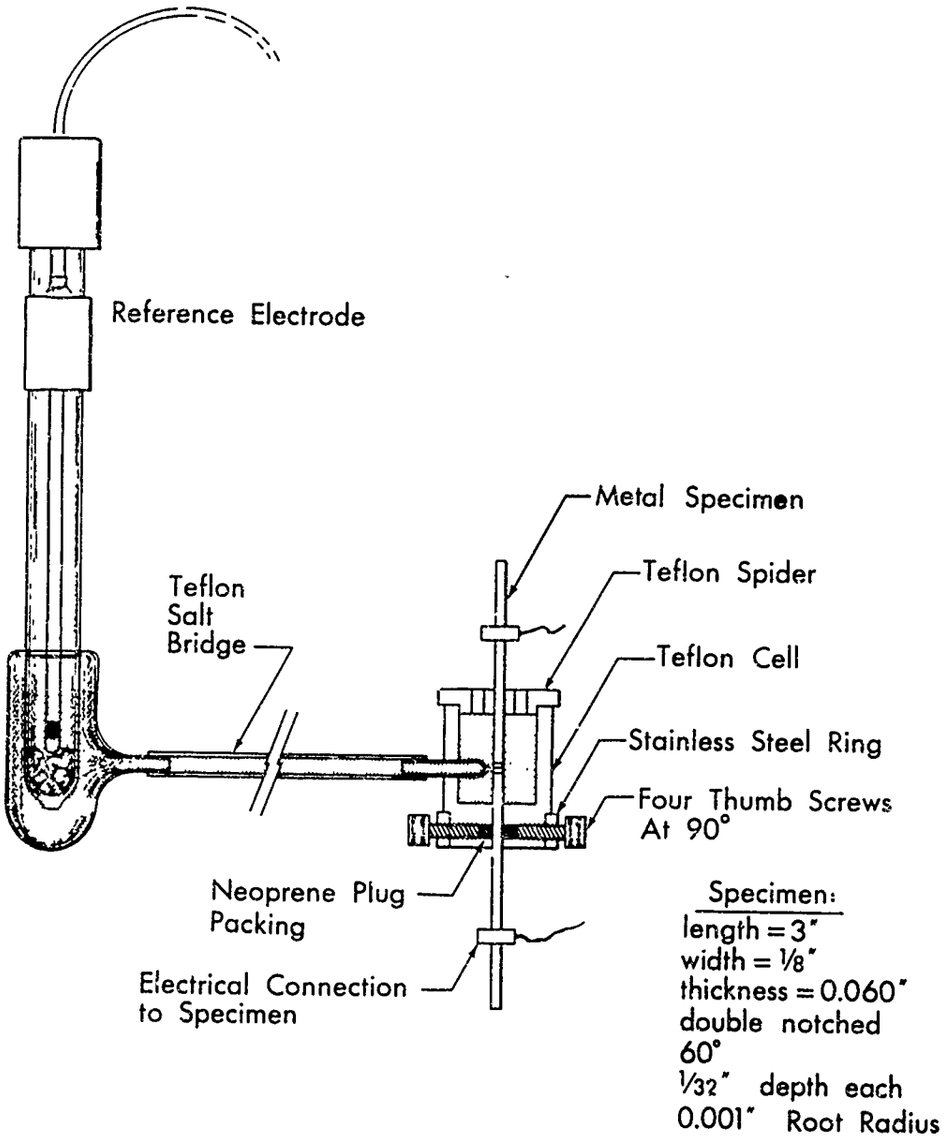

Fig. 5 Cell for kinetic experiments.

for reproducibility. It was found that electrical connection had to be made directly to the specimen, top and bottom, to avoid chattering and noise at fracture with the smaller contact area to the jaws.

RESULTS

A. Polarization Curves

Typical potentiostatic polarization curves for titanium in various electrolytes are shown in Figs. 6 through 10. The electrode surface was natural oxide covered titanium. Some of the data are from the polarization cell illustrated in Fig. 1, and some are from current measured during the tensile tests on non-anodized specimens. Commercially pure titanium foil was used in the polarization cell and Ti:8-1-1 alloy was used in the tensile tests as indicated in Table I. A potential sweep-rate of 62.4 mv/min was used with the polarization cell. The effect of pH on the reversible electrode potential is shown in Table II for reference.

Polarization of commercially pure titanium in 1 normal (1N) sulfuric acid is shown in Fig. 6. Results are compared to data reported by Stern and Wissenberg 1959, for titanium in 20% (4.7 N) sulfuric acid. Passivity was observed, as did Stern and Wissenberg, at positive potentials. Hydrogen evolution was likewise observed at potentials more negative than -800 mv. In the intermediate potential region Stern and Wissenberg observed a maximum anodic corrosion current for titanium. A cathodic current was observed in this region in the present experiments, indicating a reducible species which masked the titanium corrosion current. Reduction of oxygen is suspected as described for Fig. 8. Stern and Wissenberg used a hydrogen atmosphere in their experiments.

pH	0	7	14
E_{H_2}	- 240	- 650	-1060
E_{Ti/TiO_2}	-1100	-1510	-1920

Table II. Reversible Potential of Hydrogen Electrode (1 atm.) and Titanium-Titanium Dioxide Electrode vs pH - MV vs Saturated Calomel Electrode (SCE) Reference (From Latimer, 1952)

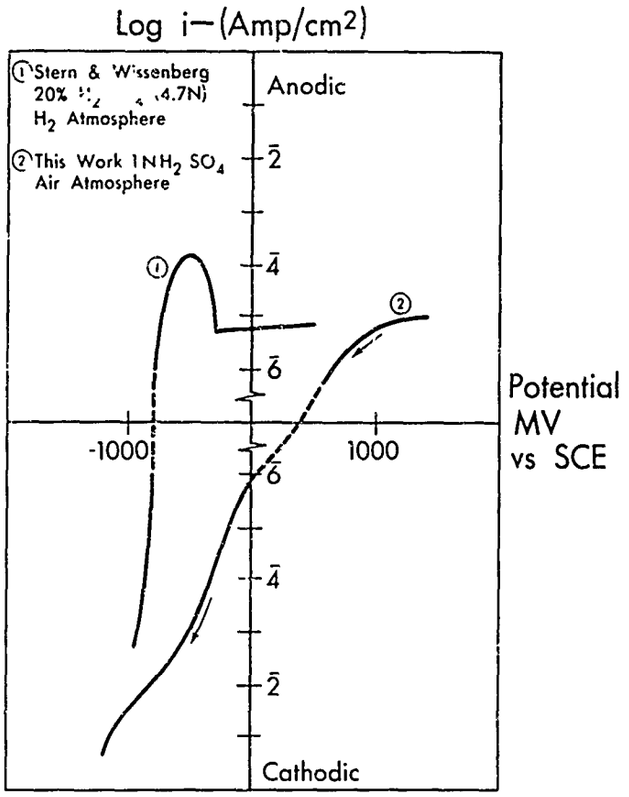

Fig. 6 Polarization curves for titanium in sulfuric acid.

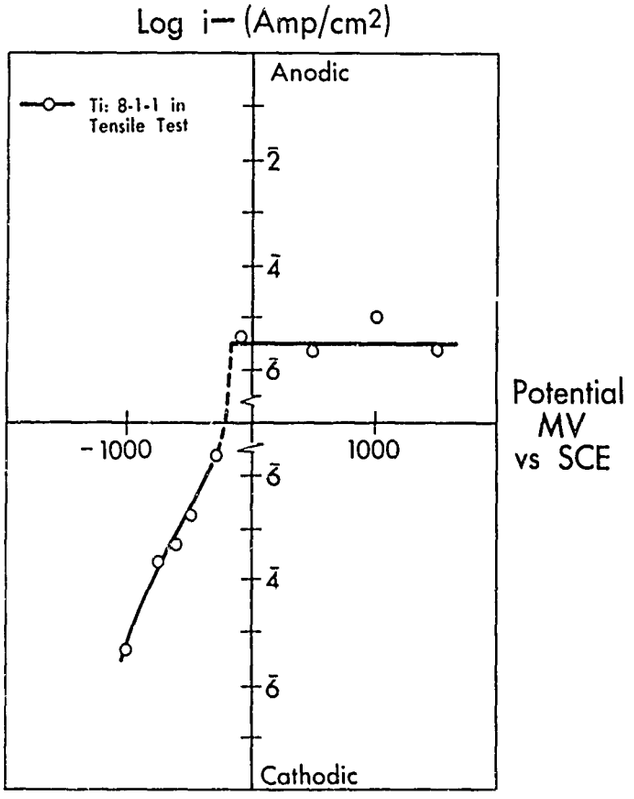

Fig. 7 Polarization curve for Ti:8-1-1 in 0.6M hydrochloric acid.

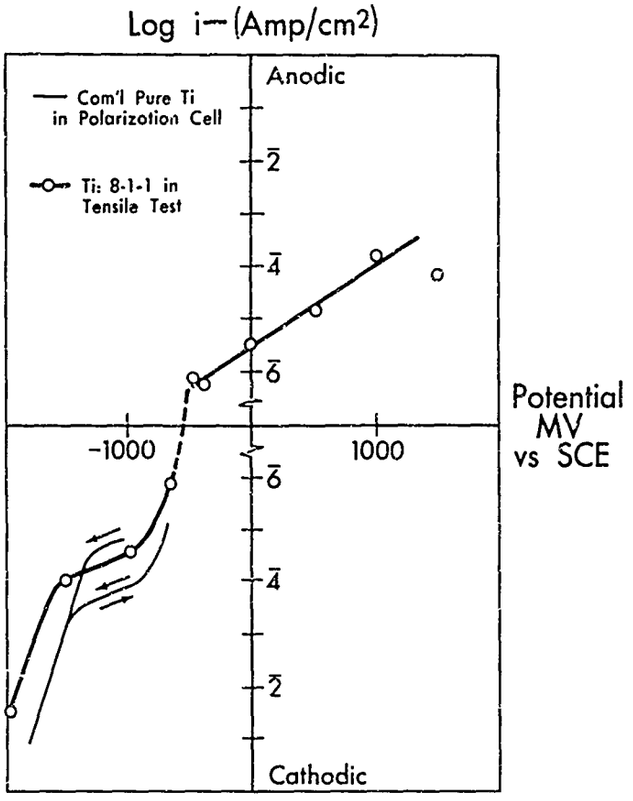

Fig. 8 Polarization curves for titanium and Ti:8-1-1 in 0.6M potassium hydroxide.

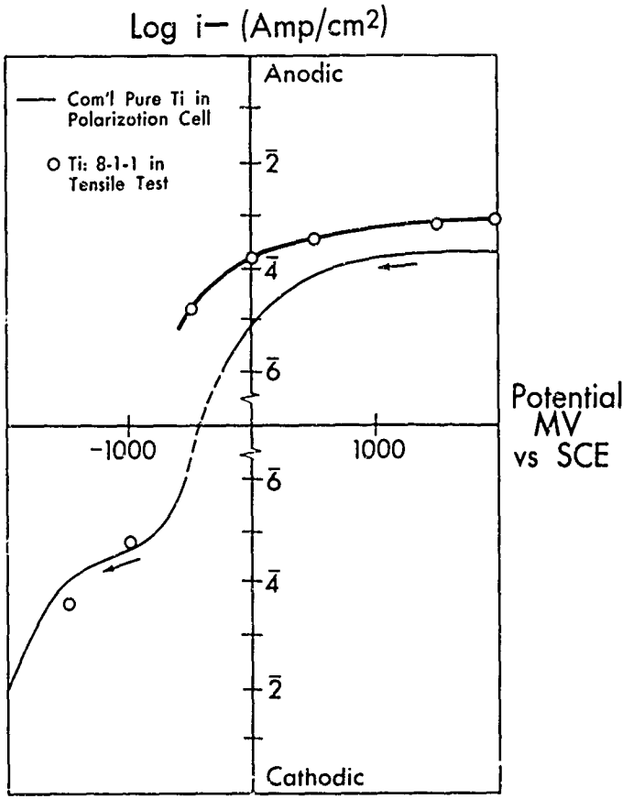

Fig. 9 Polarization curve for titanium and Ti:8-1-1 in 0.6M sodium fluoride.

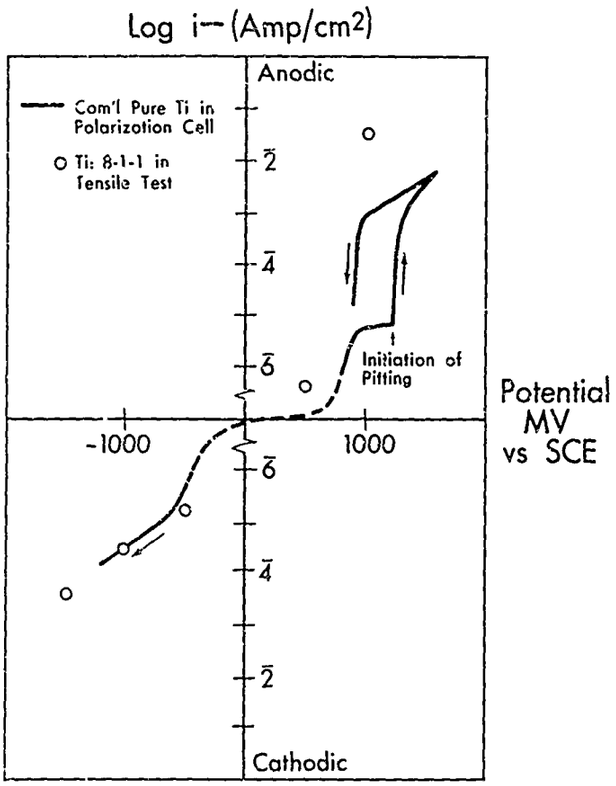

Fig. 10 Polarization curve for titanium and Ti:8-1-1 in 0.6M potassium bromide.

Polarization in 0.6 molar (0.6 M) hydrochloric acid is shown in Fig. 7 for Ti:8-1-1 tensile specimens. Passivity is shown at positive potentials. The corrosion current in the passive region was similar for neutral chloride solutions.

Polarization in 0.6 molar potassium hydroxide is shown in Fig. 8. The corrosion current appears to be higher at positive potentials in the passive region. On the cathodic side the effect of the reducible species, probably oxygen, can be seen on commercially pure Ti. The branch of the curve for increasing negative potentials was made after argon had been bubbled through the solution for an hour. The branch for increasing positive potential was after oxygen had been evolved for some minutes at the counter electrode. Immediate reversal reproduced the same branch of the curve, showing that argon had previously purged something from the cell that was produced by electrolysis.

Corrosion current in the passive region was considerably higher in sodium fluoride solution as shown in Fig. 9. The Ti:8-1-1 specimens also formed black particulate on the surface, indicating differential corrosion of the alloy components or formation of dark oxides of molybdenum and vanadium.

The initiation of pitting corrosion in bromide solutions is shown in Fig. 10 by a large jump in current in the passive region. Pitting of two 1/8 inch wide strips of commercially pure titanium is illustrated in Fig. 11. Pitting of the lower specimen was initiated at +1200 mv in the polarization experiment shown in Fig. 10. Pitting of the upper specimen was initiated at a higher potential. The mini-

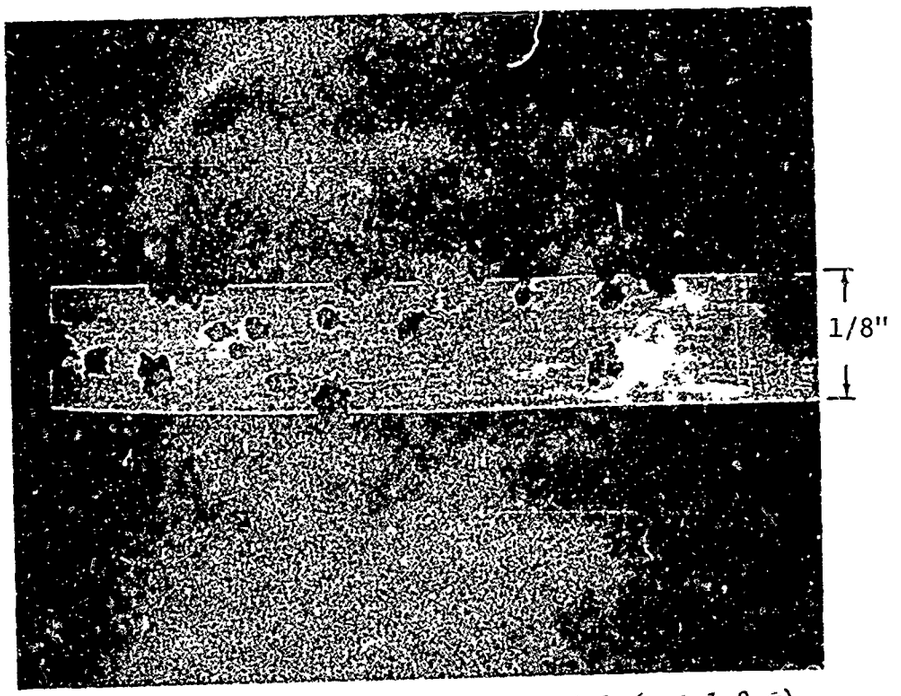

Pitting initiated at higher potential (> + 1.2 v)

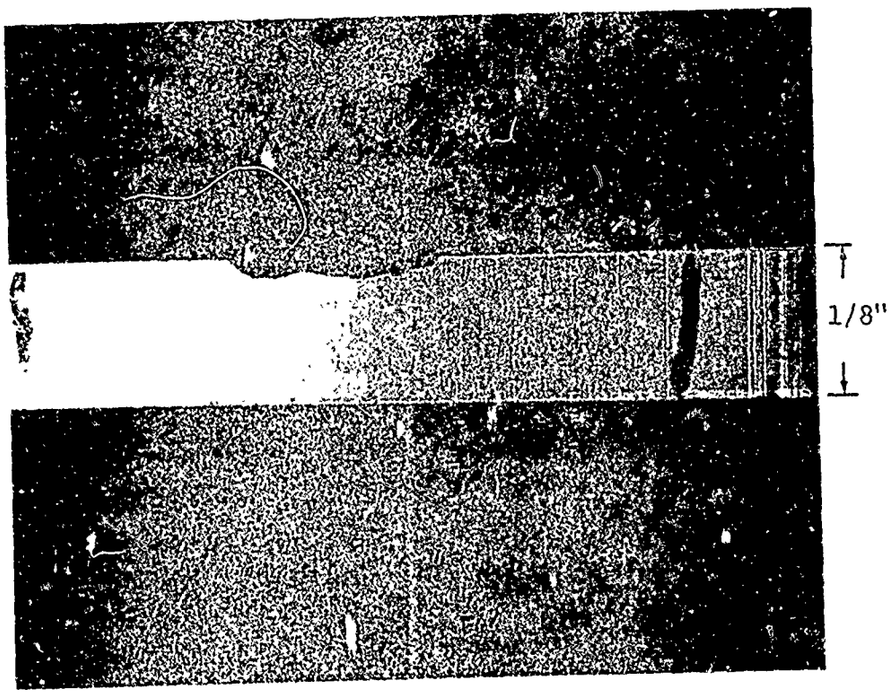

Pitting initiated at + 1.2 v vs SCE

Fig. 11 Pitting corrosion of commercially pure titanium.

mum potential for initiation of pitting appears to be between +900 and 1000 mv. A flocculent white precipitate formed in solution during the pitting corrosion experiments. This indicates that the initial corrosion product, a titanium bromide, is soluble in the electrolyte and escapes from the electrode before it hydrolyzes to the oxide or hydroxide. This was considered as an important observation to development of a model for stress corrosion cracking of titanium alloys.

B. Tensile Tests

1. Load-Time Curves

Typical load-time curves for single-notched duplex annealed Ti:8-1-1 specimens are shown in Fig. 12. Failure in 0.6 M potassium chloride is compared to that in air. The ultimate force, U_S, at failure in potassium chloride solution at a titanium potential of -500 mv is considerably less than the ultimate force, U_A, in air. The typical appearance of fracture in salt solutions under SCC susceptible conditions is shown in Fig. 13. The fracture is initially square under SCC conditions, later changing to slant shear failure. In air, the duplex annealed Ti:8-1-1 specimens failed almost entirely in slant fracture. The period of propagation of square fracture in NaCl is designated by B and the period of slant fracture by C in Fig. 12. Most specimens were preloaded to 1000 Kg (2200 lbs) as shown, in order to save time. The first visible evidence of a plastic zone by appearance of a dimple on the surface around the root of the notch occurred at 1300 to 1500 Kg.

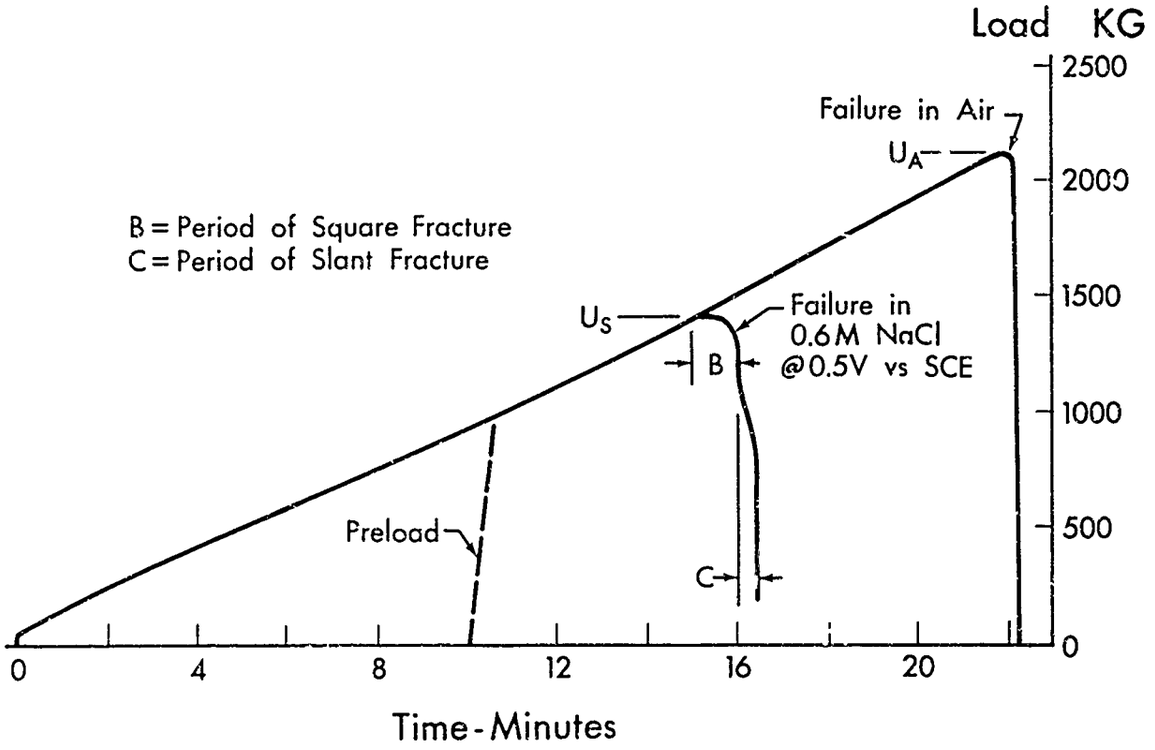

Fig. 12 Load-time curves for single-notched duplex annealed Ti:8-1-1 specimens.

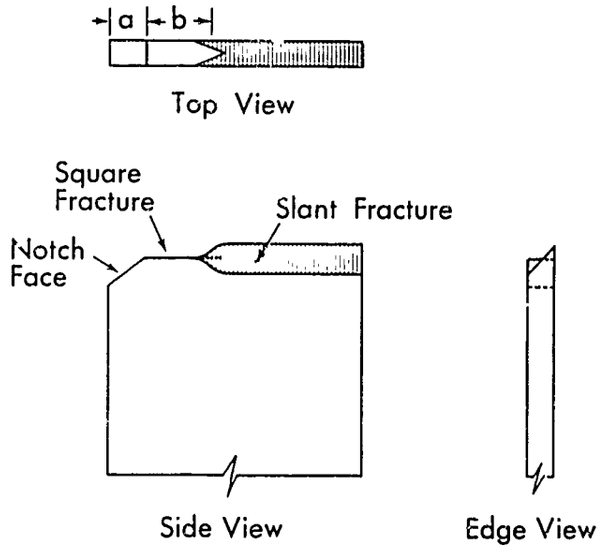

Fig. 13 Typical appearance of fracture.

2. Current-Time Curves

A typical plot of current flowing under SCC conditions is given in Fig. 14. In the period, A, before SCC commences, the current measured is that flowing to the old exterior surface of the specimen. This current may be anodic or cathodic depending on the salt solution and applied potential. It is this current that is plotted as the experimental points from the tensile tests in Figs. 7 through 10. Later specimens were anodized to minimize this background current. When stress corrosion cracking started, the current jumped in the anodic direction designated by the region B, in Fig. 14. Transition to the shear mode or slant failure, region C, was accompanied by a peak in current. The peak correlated with the observed change on the specimen surface from square to slant fracture. A high anodic current accompanied the final failure. Time for propagation of square fracture could be directly measured from the current-time plots, which were made for every run. In cases where the background current in period A was large, either anodic or cathodic due to high positive or negative polarization, the crack propagation current and time were sometimes obscured.

A typical pattern of current versus time under a potential giving immunity to stress corrosion cracking is shown in Fig. 15. The first evidence of anodic current pips is difficult to define but there was generally a peak at point X followed by a long period of an irregular current of a few microamperes until slant failure occurred. Point X generally occurred at a load of about 1400 Kg for the single-

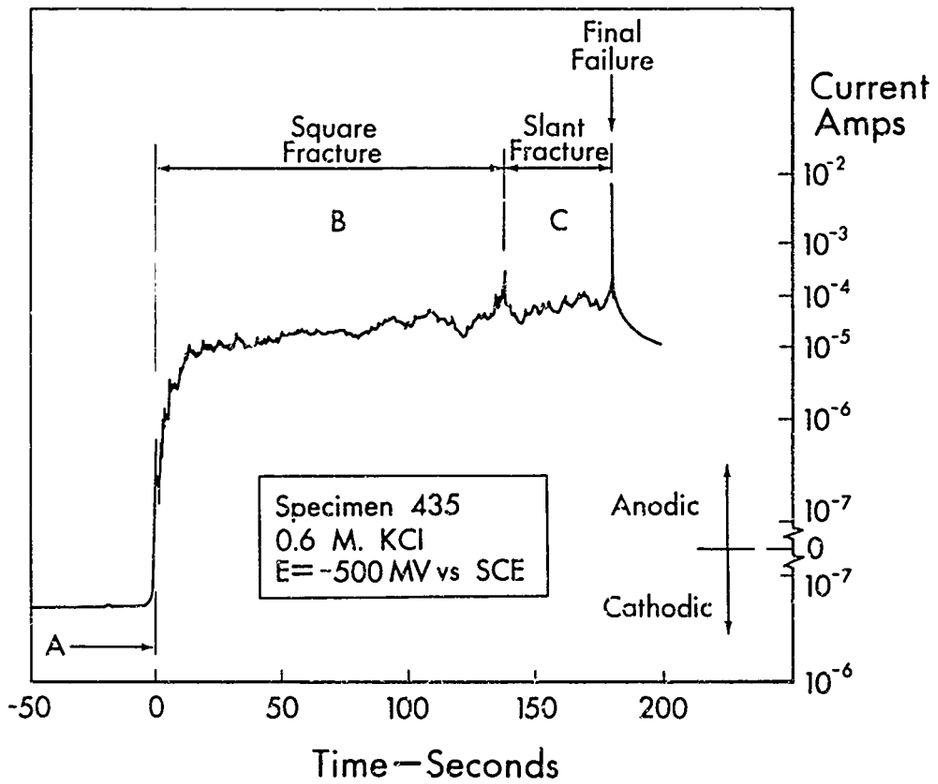

Fig. 14 Typical current versus time relation under SCC conditions.

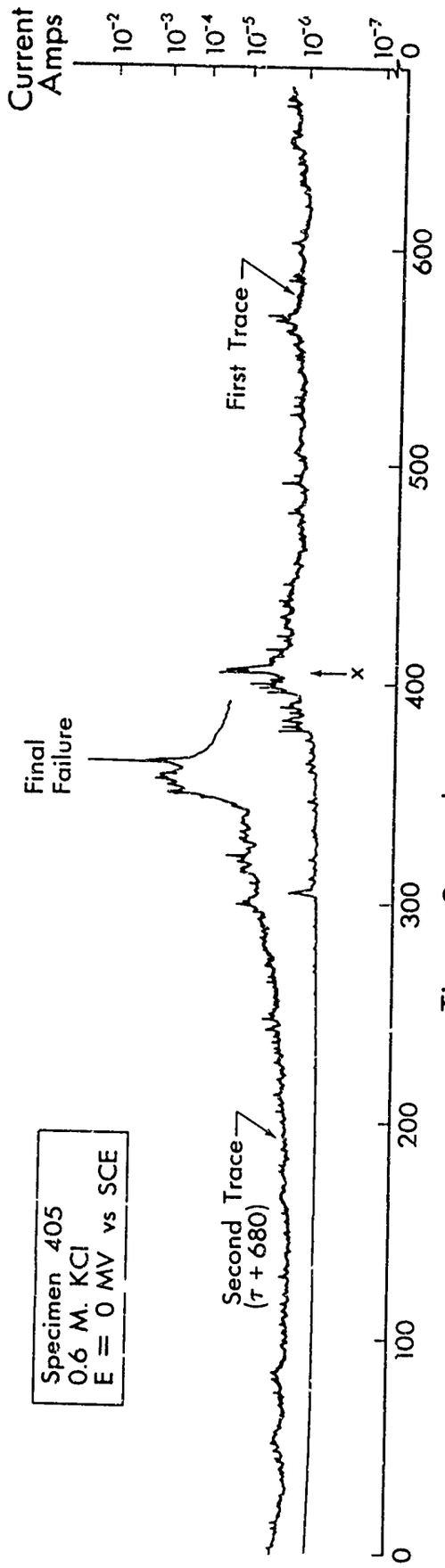

Fig. 15 Typical current versus time relation under non-SCC conditions.

notched duplex-annealed Ti:8-1-1 specimens. The irregular anodic current is presumably due to anodizing of metal in cracks in the oxide film in the plastic zone around the root of the notch. Because of its low value, this current was easily obscured by current flowing to the old surface.

3. Effect of Crosshead Velocity

Early in the program, the effect of crosshead velocity was investigated in order to determine a suitable value to use in the tests. Results are shown in Fig. 16 for double-notched, duplex-annealed Ti:8-1-1 specimens in air and in 0.6 M sodium chloride at a potential of -500 mv. The strengths plotted are the ultimate values, U_A and U_S, illustrated in Fig. 12. Stress corrosion cracking appeared to occur at crosshead velocities of less than 10^{-1} cm/min. A velocity of 5×10^{-3} cm/min was chosen as standard for all subsequent tests as this gave measurable differences in a short period of time.

The stress shown at the right of Fig. 16 was based on the notch section area. The un-notched specimens with slightly higher strength had the same net cross section as the notched specimens at the notched section indicating that duplex annealed Ti:8-1-1 is slightly notch sensitive. There appears to be reasonable agreement of tensile strength of the un-notched specimens to the data in Table I for duplex-annealed Ti:8-1-1.

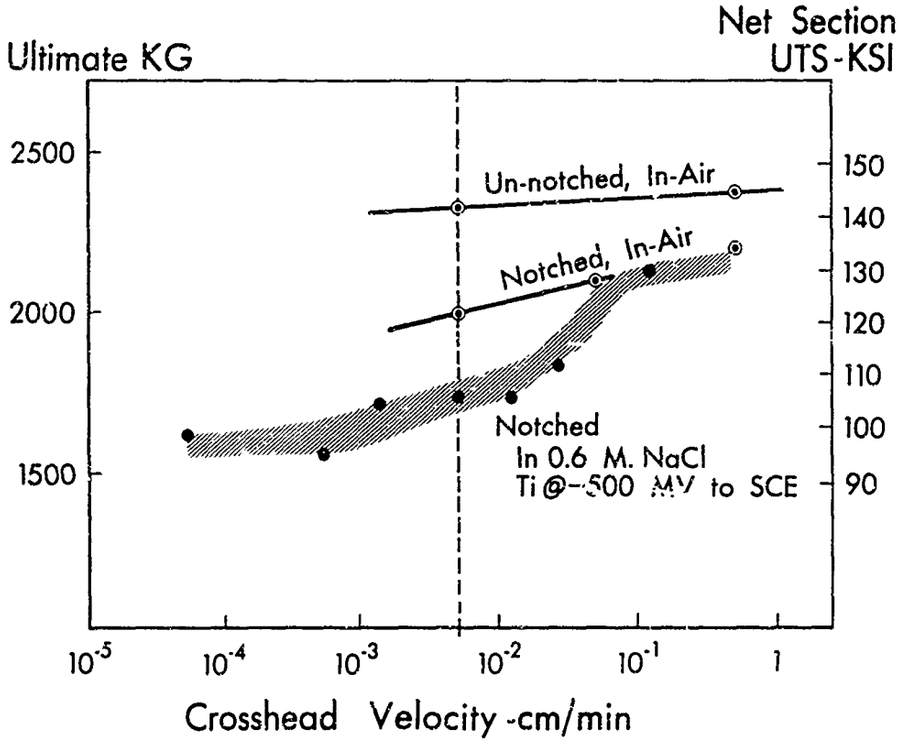

Fig. 16 Effect of crosshead velocity for double-notched, duplex-annealed Ti:8-1-1.

4. Effect of Notch Radius

The effect of notch radius was investigated in order to specify the tolerance on the machining of the notches and to determine variability in results due to this factor. Double-notched specimens of duplex-annealed Ti:8-1-1 alloy were machined with notch root radii of 1, 2, 5 and 20 mils (0.0025, 0.005, 0.012 and 0.05 cm) for these tests. Two specimens had a notch root radius of about 0.5 mils (0.0012 cm), produced by pressing a knife blade into a 1 mil radius notch.

Results in air and 0.6 M lithium chloride, potassium bromide and potassium iodide solutions are shown in Fig. 17. The results in air and in LiCl at a potential +1000 mv were within the same scatter-band and indicated some notch sensitivity. Specimens in LiCl at -500 mv showed SCC susceptibility for notch radii below 10 mils, but SCC immunity for larger radii. All specimens with notch radii in the range of 1 to 20 mils were susceptible in KBr and KI at a potential of +1000 mv. Two specimens with 20 mil notch radius were electro-polished in the notches and tested at +1000 mv in KI solution and little or no sensitivity was indicated.

It was decided, based on these tests, to use 1 mil radius machined notches as standard.

5. Effect of Halide Ions

Stress corrosion cracking of Ti:8-1-1 alloy in aqueous environments at room temperature has been found to be very specific to three

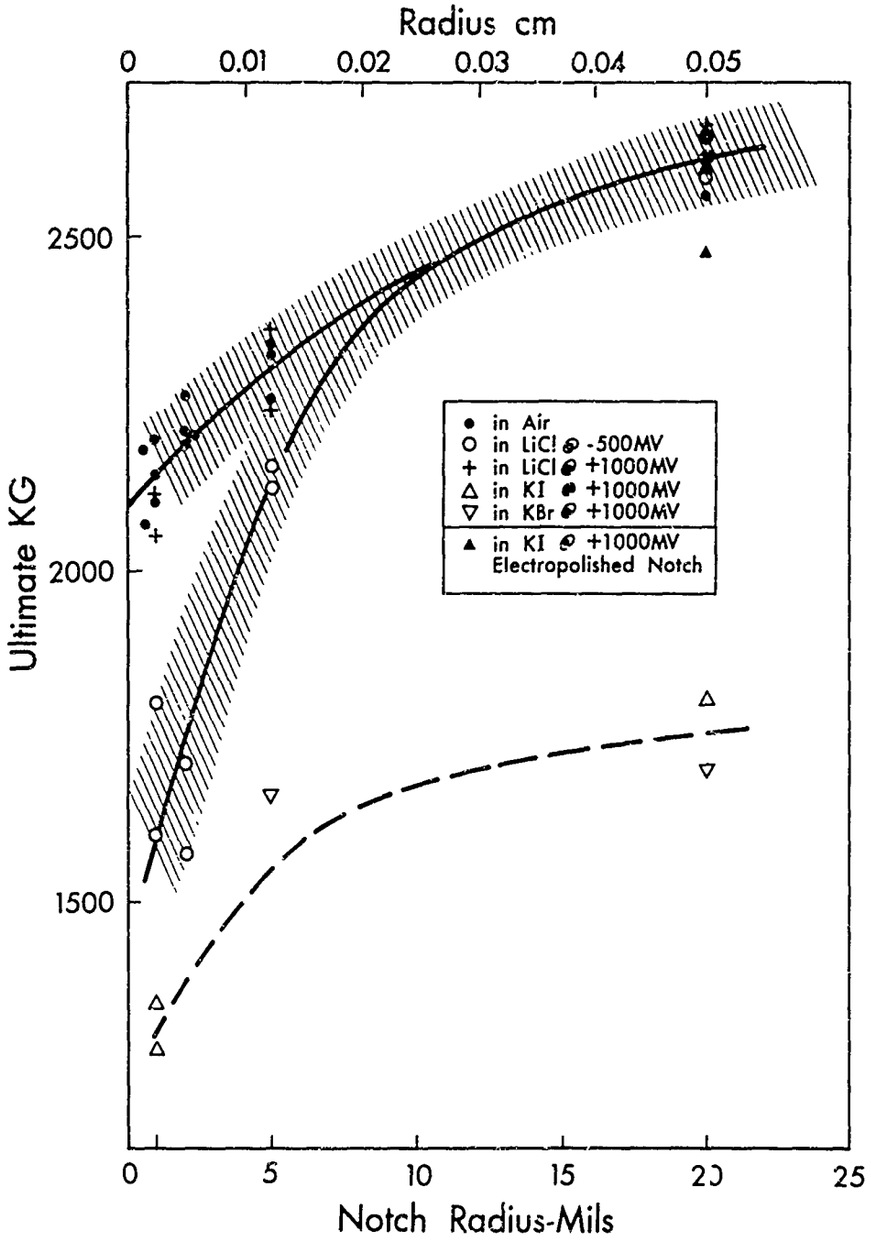

Fig. 17 Effect of notch root radius on ultimate strength.

ions; chloride, bromide and iodide, and to date no others. Other anions investigated were fluoride, hydroxide, sulfide, sulfate, nitrite and perchlorate. There also appeared to be no cation effect within the limits of accuracy of the experiments. The ultimate load versus potential for neutral fluoride, chloride, bromide and iodide is given in Fig. 18. The experimental points are not shown on this and some other plots of ultimate strength for purpose of clarity. The scatterband width is indicated in the lower left of Fig. 18.

At potentials more negative than about -1000 mv, the specimens appeared to be cathodically protected in all solutions. At all potentials, the NaF solution gave results in the same scatterband as the air values. At potentials more positive than -1000 mv, SCC susceptibility in varying degrees occurs in chloride, bromide and iodide solutions. A region of anodic protection occurs in chloride and bromide solutions. Pitting corrosion and flocculent white precipitate were observed at +1000 mv in KBr solution and +2000 mv in LiCl solution. A photograph of a specimen failed in 0.6 M KBr solution, Fig. 19, shows the pits and short radial lines on the surface that appeared to be normal to the stress direction around the notches. The pits contained black material that presumably was molybdenum and vanadium oxides. Although there was a decrease in strength in KI solution at about +700 mv, no pitting or white precipitate were observed.

The ultimate strength shown in Fig. 18 is actually a measure of the stress for initiation of stress corrosion cracking. This is illustrated in Fig. 12, where it is shown that the ultimate load is

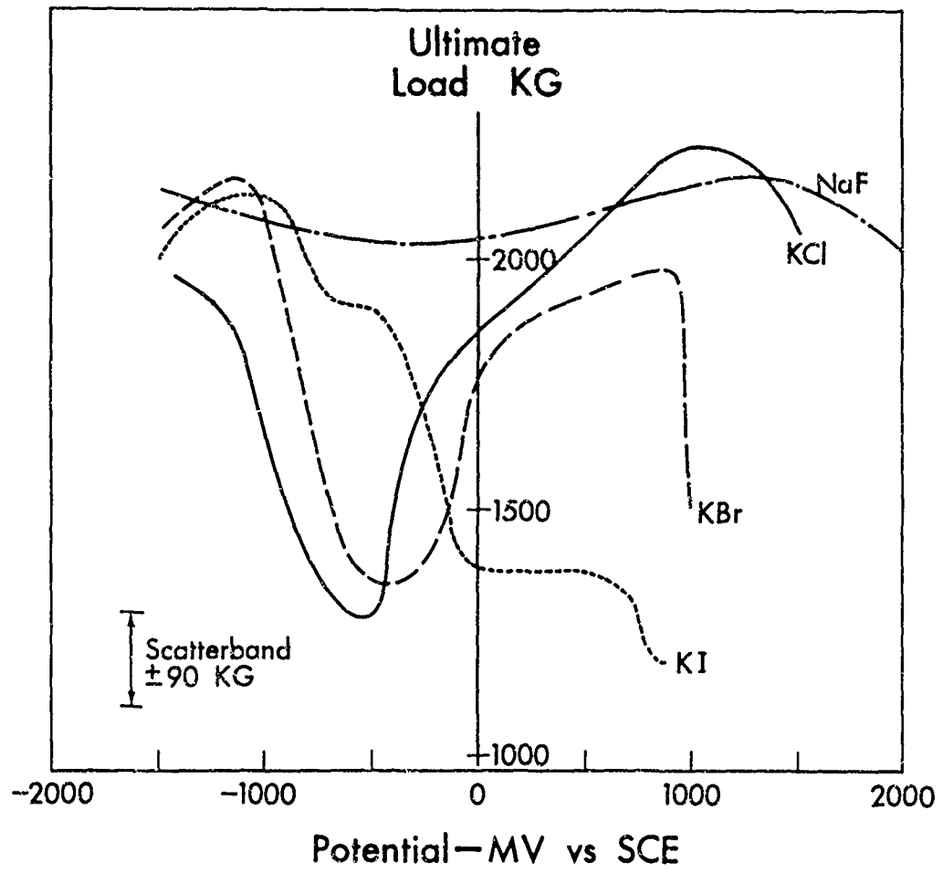

Fig. 18 Ultimate load versus applied potential in 0.6M halide solutions.

Fig. 19 Specimen failed in 0.6M potassium bromide at +1000 mv (specimen 37).

very little higher than the load for initiation. Propagation is, however, related to initiation. It was found, for example, that SCC could be initiated at -500 mv in chloride solution and stopped by switching the potential to either the anodic or cathodic protection zone. It was also found that SCC could be initiated at higher loads than normal at -500 mv by first loading in the anodic or cathodic protection zone to a point approaching failure at that potential and then switching to -500 mv.

The power of the potentiostatic technique is demonstrated in Fig. 18. Specimens on open circuit have a rest potential that is variable depending on metal composition, history of the surface, trace impurities in solution, etc. A range of at least +500 to -500 mv has been observed on titanium. In this range many changes occur, accounting in part for the large variability in strength observed by others under open circuit conditions.

6. Crack Propagation Velocity and Associated Current

Crack propagation velocity was measured by two means: 1. by visually observing the progress of the crack past scribed pencil lines on a specimen surface, and 2. by dividing the square-fracture length (b in Fig. 13) by the square-fracture time (B in Fig. 14). A comparison of the two methods is shown in Fig. 20. There appeared to be reasonably good agreement for this specimen at -500 mv in 0.6 M LiCl.

It would have been desirable to make all velocity correlations

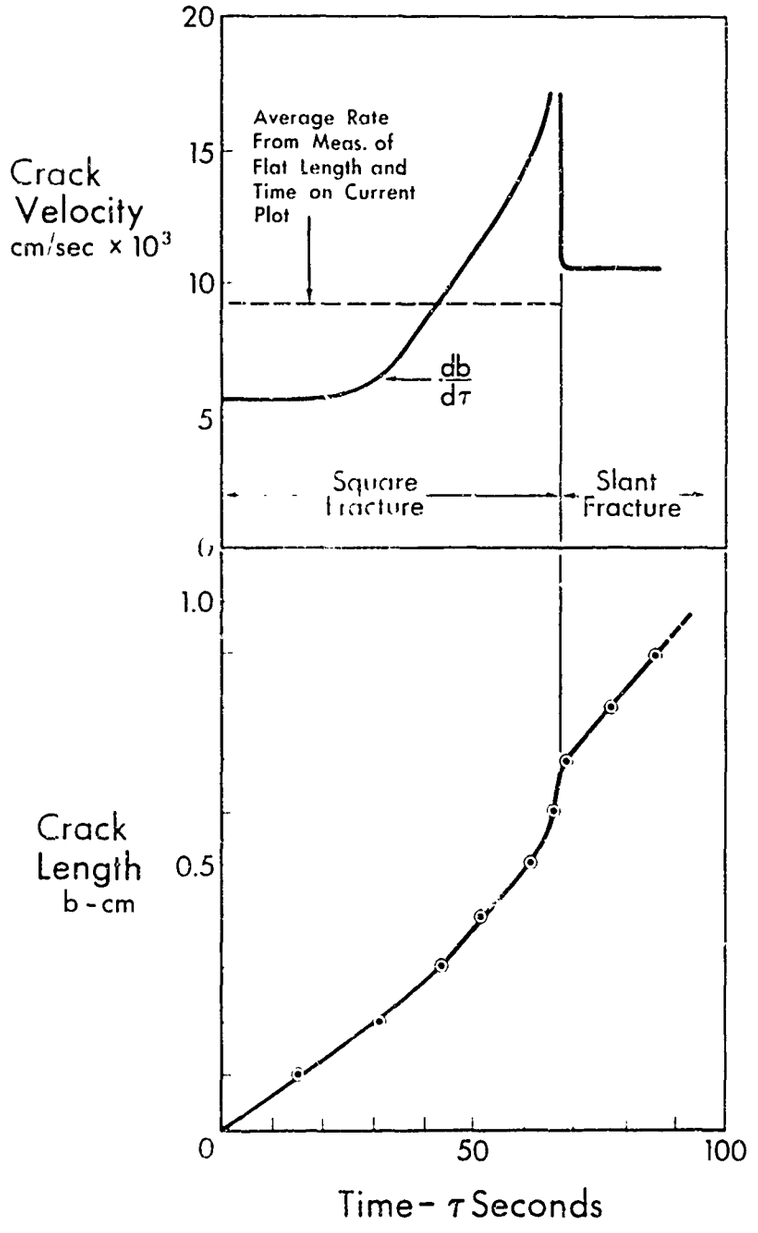

Fig. 20 Crack length and velocity versus time (specimen 155).

using initial crack velocity from visual observation of crack length. This was a tedious measurement and only a few were made. Data were available, however, from the experiments already made to calculate average crack velocity. If the ratio of average velocity to initial velocity is relatively constant, correlation using average velocity appears justified at this time.

Average crack propagation velocity was found to be linear with applied potential in 0.6 M chloride, bromide and iodide solutions for those specimens that failed below 1500 Kg load. These data, based on square fracture length and time, are plotted in Fig. 21. This is probably one of the more significant findings in this work thus far, as it demonstrates that, once initiated, the crack propagation velocity is determined by the electrochemistry.

The current during square-fracture crack propagation as measured from current versus time plots such as shown in Fig. 14 is plotted in Fig. 22. The average initial current and the average final current just before initiation of shear fracture appear to be linear with applied potential. The average current was estimated by drawing by eye a horizontal line through about 30 seconds of the wiggly current plot. That the ratio of final current to initial current appears to be constant up to at least zero mv to SCE lends some assurance that the correlation using average velocity was justified.

The values of the intercepts on the potential axes in Figs. 21 and 22 play an important role in the analysis presented in the Discussion. The intercepts in Figs. 21 and 22 are -900 mv and -850 mv,

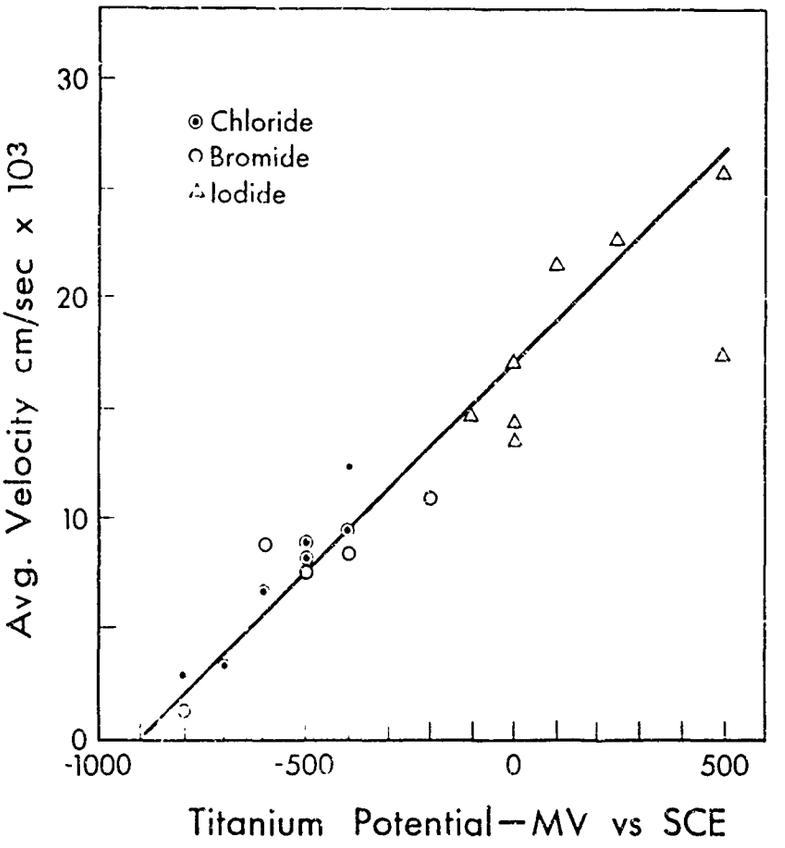

Fig. 21 Relation of average crack propagation velocity to applied potential in 0.6M halide solutions.

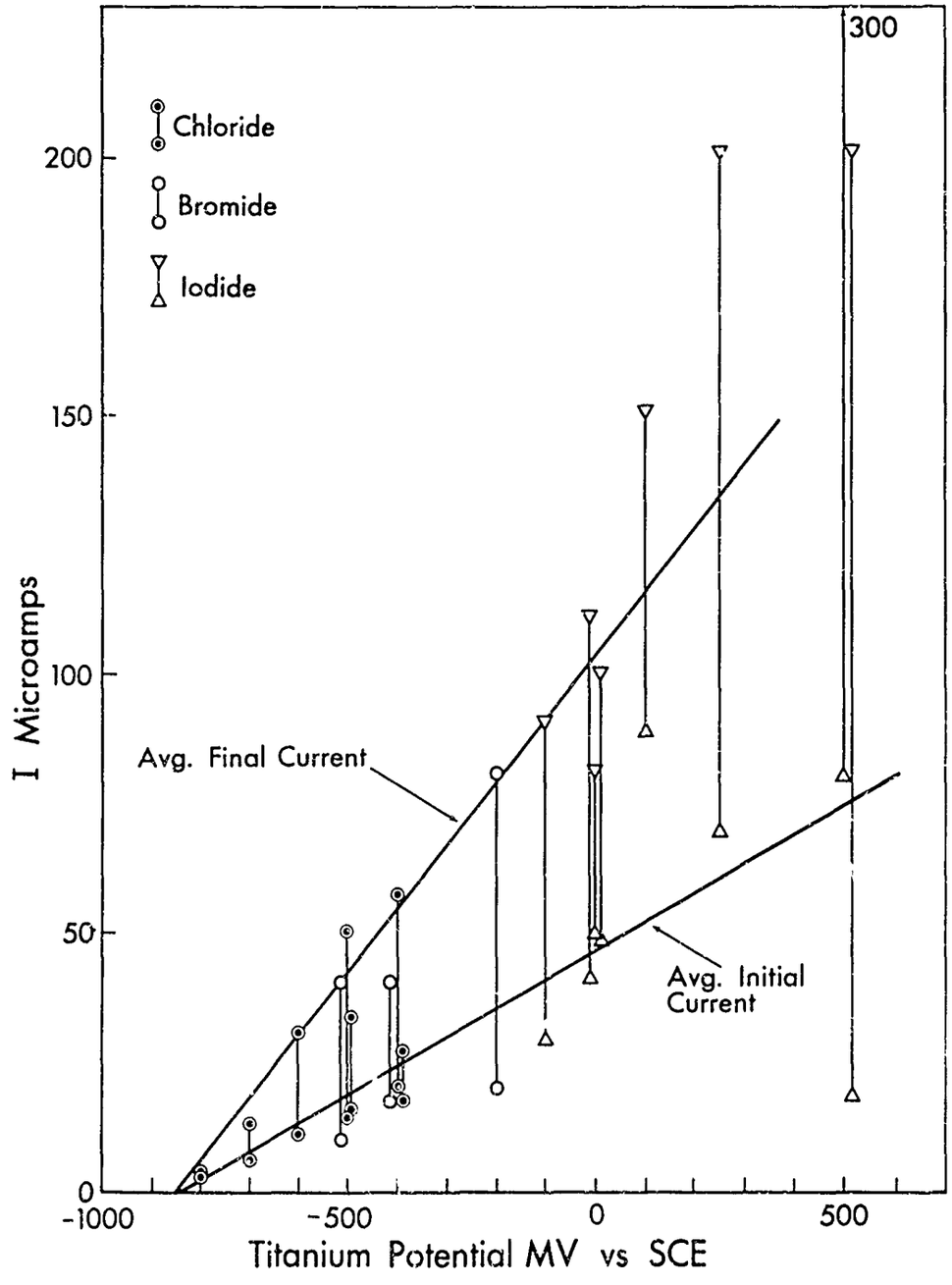

Fig. 22 Relation of crack propagation current to applied potential in 0.6M halide solutions.

respectively. Because there is reason for believing that they should be identical and because the measured current shown in Fig. 22 had a large scatter, an average value of -900 mv will be used in the Discussion.

7. Effect of Concentration

The effect of concentration of hydrochloric acid in water on ultimate load versus potential is shown in Fig. 23. Each curve was established with only 10 to 14 points so that the accuracy of the curves is limited, but two trends are observed:

1) The potential at which SCC susceptibility begins on the negative side appears to be relatively independent of concentration.

2) The potential for initiation of anodic protection increases with decreasing concentration. The value of the minimum ultimate load near -500 mv also appears to be a function of concentration.

In the data of Fig. 23 the pH and the electrolyte conductivity varied widely as well as the chloride ion concentration. A series of experiments was therefore run at a relatively constant pH and electrolyte conductivity but variable chloride ion concentration. The results of these experiments are shown in Fig. 24 for potassium hydroxide - potassium chloride solutions. An alkaline solution was used with the objective of excluding the possible hydrogen mechanisms in SCC. The 0.6 M KCl in 0.6 M KOH solution gave essentially the same results as

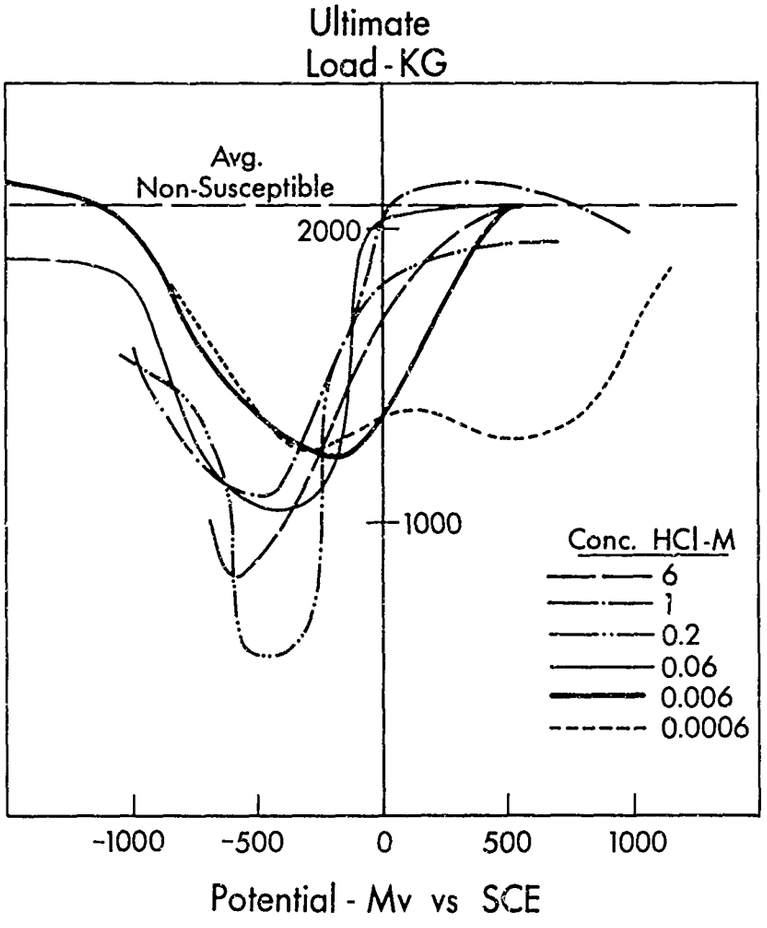

Fig. 23 Effect of concentration of HCl on ultimate load.

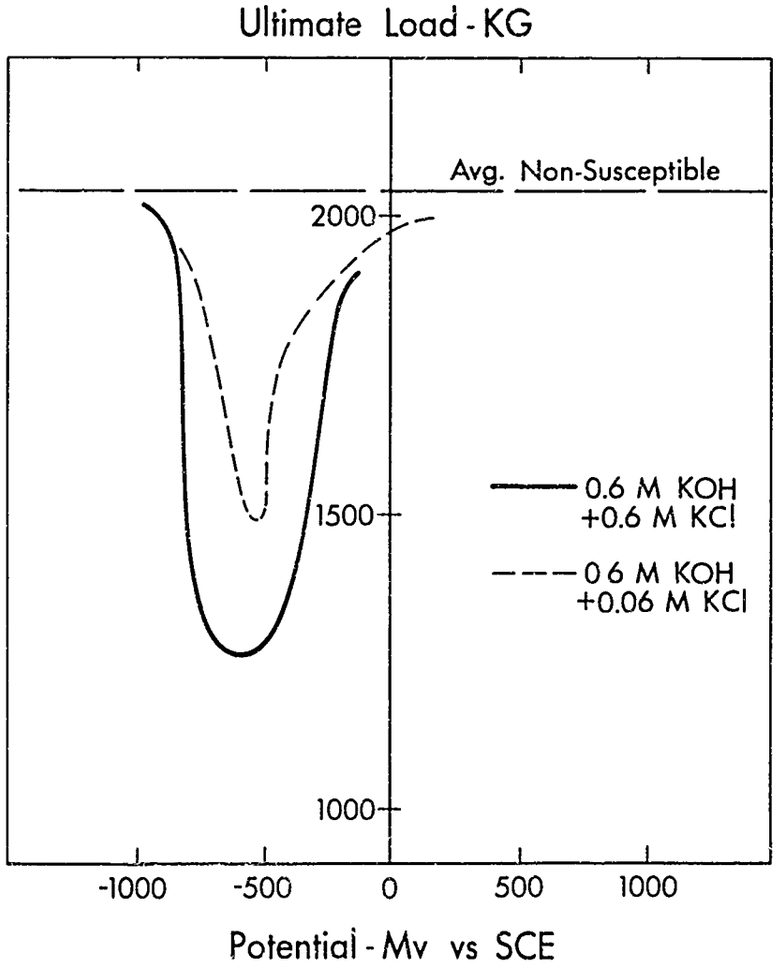

Fig. 24 Effect of chloride concentration on ultimate load in alkaline solutions.

0.6 M KCl alone. The zone of SCC susceptibility decreased in 0.06 M KCl in 0.6 M KOH solution and disappeared in 0.006 M KCl in 0.6 KOH.

A further demonstration of the SCC inhibiting effect of hydroxyl ion is shown in Fig. 25. Potassium hydroxide did not inhibit the SCC of Ti:8-1-1 alloy in 0.6 M potassium iodide solution at +200 mv until the concentration reached about 1.5 M in KOH. Inhibition then increased with concentration. Eight molar sodium perchlorate partially suppressed the SCC in 0.6 M sodium iodide solution and decreased the crack propagation rate.

The ultimate strength of Ti:8-1-1 alloy at -500 mv in mixtures of 0.6 molar sodium fluoride and chloride are shown in Fig. 26. There was no change in pH and little change in conductivity. A relatively large excess of fluoride appears to be necessary for suppressing SCC.

8. Effect of Temperature

Temperature of the specimen and electrolyte from 0° to 74°C had little effect on ultimate load or crack propagation velocity within the limits of experimental error in chloride electrolytes with specimen at -500 mv as shown in Table III. The temperature of 0°C was obtained by pouring liquid nitrogen into the cell until the surface of the electrolyte froze to ice around the specimen. The 74°C temperature was obtained by shining heat lamps on the specimen and cell and controlling temperature with an epoxy insulated thermocouple in the electrolyte. As the temperature effect was not large compared to temperature effects on

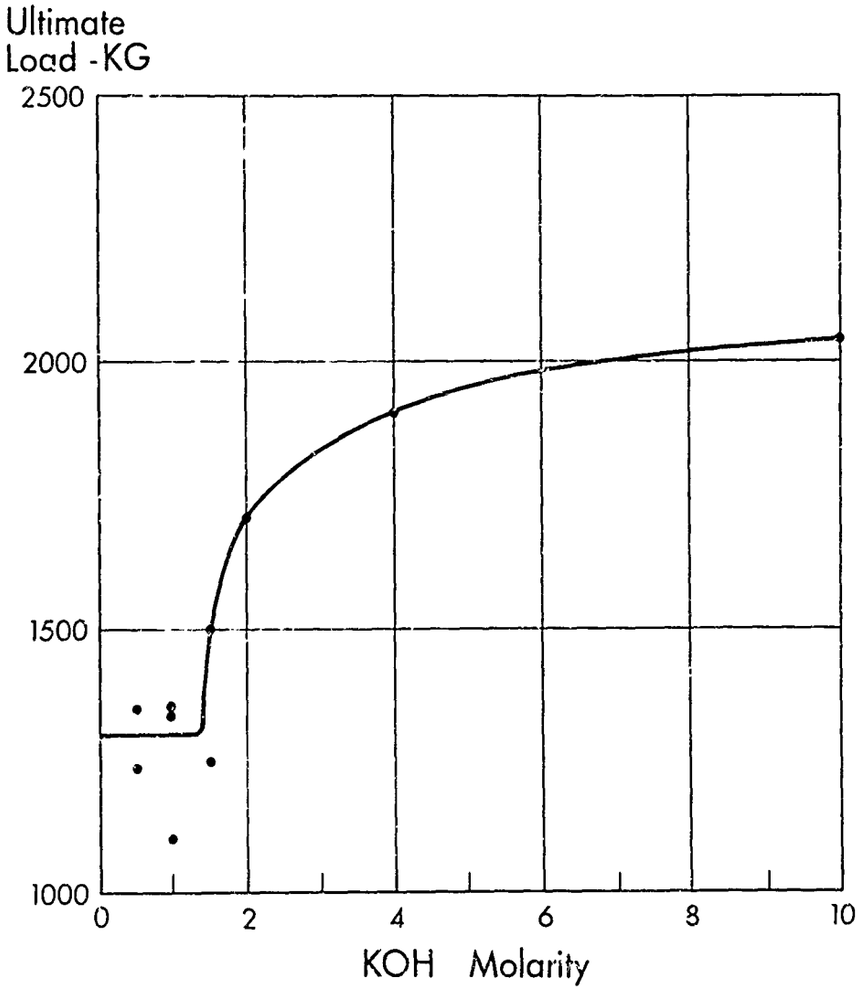

Fig. 25 Effect of potassium hydroxide concentration in 0.6M potassium iodide on ultimate load at +200 mv.

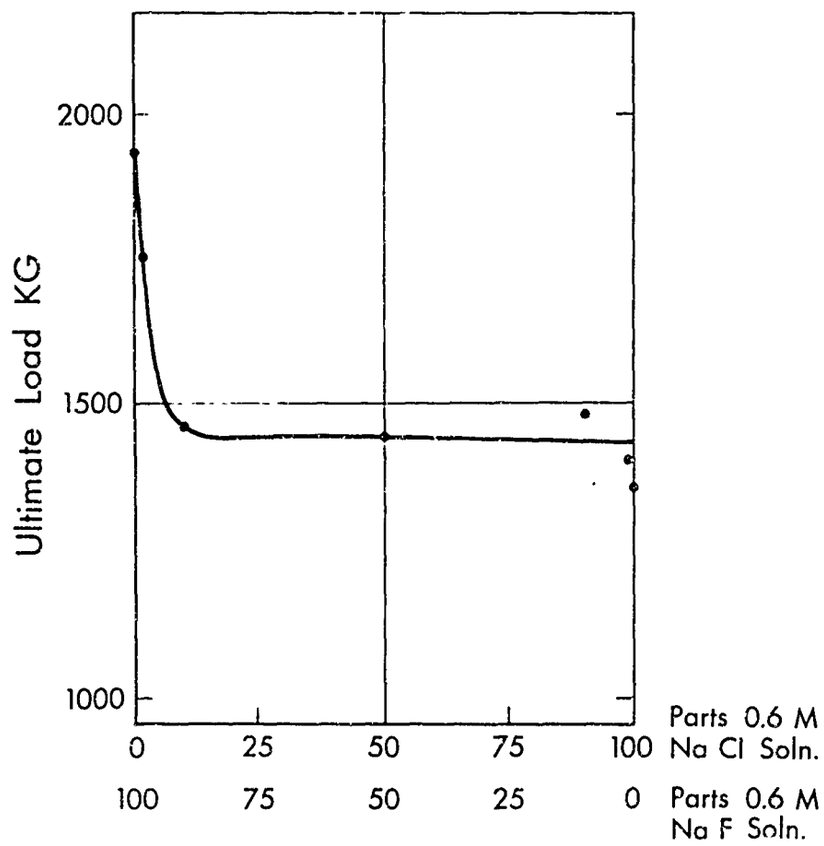

Fig. 26 Effect of relative NaCl - NaF concentrations on ultimate load at -500 mv.

Specimen No.	Electrolyte	Temp °C	Ultimate Load-KG	Crack Velocity cm/sec x 10^3
473	0.6 M KCl	0	1500	4.6
Avg. of Several Specimens	0.6 M KCl	21	1300±90	8
145	0.6 M LiCl	74	1340	5.0*

* Velocity could be larger than this value because time of transition to shear could not be determined.

Table III Effect of Temperature on Ultimate Load and Crack Propagation Velocity at Potential of -500 mv in Chloride Solutions

chemical kinetics, further experiments were postponed.

9. Effect of Heat Treatment

A series of experiments was conducted to investigate the effect of heat treatment of Ti:8-1-1 and the preliminary results are summarized in Figure 27. It can be seen that notched specimens of the alloy in the mill-annealed condition are relatively brittle under all conditions of test and are relatively environment insensitive. The results on duplex-annealed material have been described and in this condition the alloy shows considerable environmental and potential sensitivity. This effect is accentuated by water quenching from 800°C when the strength of the alloy is reduced by a factor of two in LiCl at -500 mv. Further heat treatment experiments are planned.

10. Fractographic Analysis

Electron photomicrographs taken of the square-fracture surface of a specimen failed at -500 mv in chloride solution and a specimen failed at +1000 mv in iodide solution showed the same pattern of transgranular cleavage of the alpha phase in Ti:8-1-1 alloy. These imply a similar process of cleavage. An example photomicrograph is shown in Fig. 28. Further fractographic analyses are planned.

C. Kinetics of Oxidation

Results of the kinetic experiments using one-inch wide 0.060 inch thick mill-annealed specimens are shown in Fig. 29. The curves

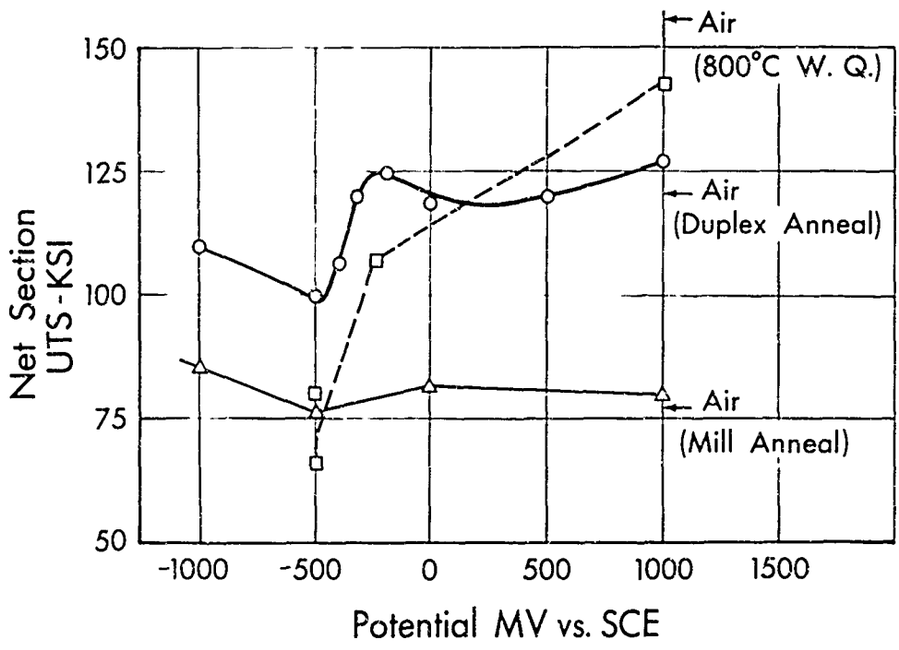

Fig. 27 Ultimate strength of Ti:8-1-1 notched 0.050" to 0.060" sheet after various heat treatments.

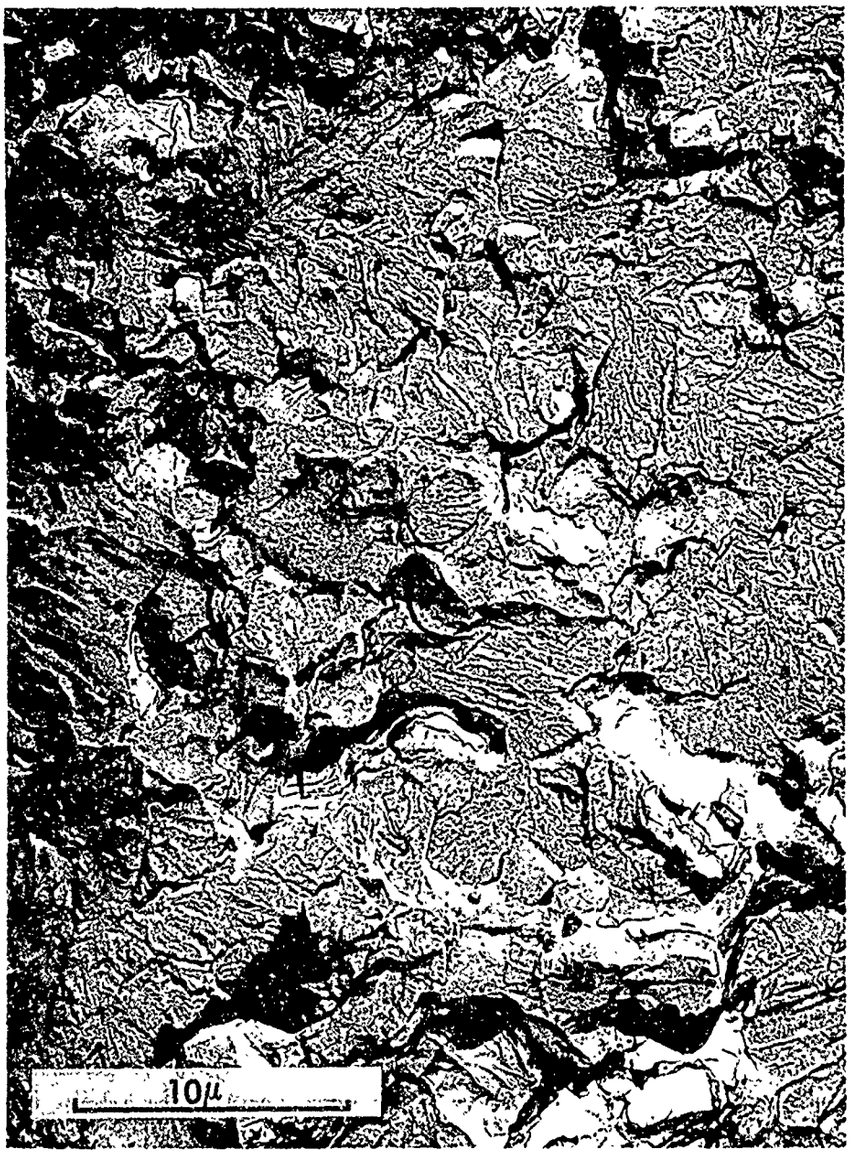

Fig. 28 Electron photomicrograph of area of square fracture surface - specimen 108 in 0.6M LiCl @ -500 mv.

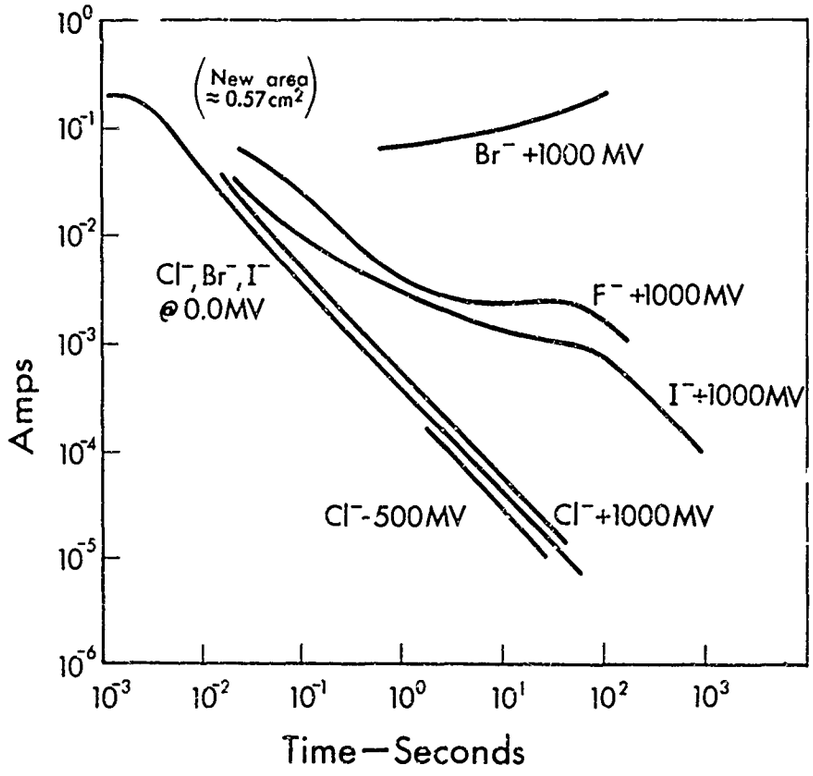

Fig. 29 Kinetic data on oxidation of Ti:8-1-1.

were plotted from x-y records and oscilloscope data from the time of final failure. At a potential of zero volts to SCE applied to the titanium specimen, the 0.6 M chloride, bromide and iodide solutions gave essentially the same current versus time relationship. The initial, approximately horizontal, part of the curve corresponds to formation of about a monolayer of oxide ions. The charge density is $\frac{2 \times 10^{-1}}{0.57}$ amp/cm^2 x 2.5 x 10^{-3} sec = 880 x 10^{-6} coul/cm^2. Monolayer coverage of oxide ion gives about 425 x 10^{-6} coul/cm^2 (Appendix C). The difference between these two values may be due to surface roughness and experimental error. Thereafter the current decays approximately with the reciprocal of time. The theory of this relationship is described in Appendix D.

From the equality of the curves, the same mechanism appears to apply for the chloride, bromide, and iodide with the specimen at zero mv to SCE. This is presumably the oxidation of titanium by water. The current versus time relation increases with increased positive potential in 0.6 M chloride as expected qualitatively from theory (Appendix D).

Considerable deviations in the direction of increased current occurred in 0.6 M fluoride, bromide, and iodide solutions at a specimen potential of +1000 mv. In the case of fluoride this is consistent with the high uniform anodic current shown in Fig. 9. At a specimen potential of zero mv to SCE in fluoride solution the current versus potential curve (not plotted) was just slightly below the one shown in Fig. 29, indicating that here also the fluoride ion participates in the

oxidation of titanium. Titanium at +1000 mv in 0.6 M bromide solution, as noted earlier, is in the pitting corrosion region. The rise of current with time is probably due to increase in number and/or size of pits. Although iodide did not show visible evidence of pits to the eye in the specimen at +1000 mv, pitting is suspected at a micro scale.

In order to determine the cause of the limiting current on the freshly fractured surface (at less than 10^{-2} sec.), smaller specimens were fractured in the cell shown in Fig. 5. Smaller specimens allowed a higher current density within the current limit of the potentiostat. It was found that the potential drop between the tip of the Luggin capillary and the specimen limited the current from the potentiostat. Moving the tip closer to the specimen or increasing the electrolyte conductivity increased the initial current.

To put the analysis in more quantitative terms, a potential balance between the reference electrode and the working electrode in Fig. 1 gives

$$E_p = E^\circ_{we} + \dot{\eta} + IR_e$$

where

E_p = input potential to potentiostat, volts.

E°_{we} = reversible potential of specimen (working electrode), volts (E°_{we} = -1.5 volts @ pH = 7, Table II).

η = overpotential, volts. (Assume zero as first approximation for new titanium surface.)

I = current to specimen, amps.

R_e = resistance of electrolyte between working electrode and tip of Luggin capillary.

For the above conditions and an initial current of 2×10^{-1} amp at $E_p = 0$ volts, $R_e = \frac{1.5}{2 \times 10^{-1}} = 7.5$ ohms. This is consistent with the approximate 0.2 cm Luggin tip to working electrode spacing and an electrolyte resistivity of about 20 ohm cm ,

$$R_e = \frac{\rho_e \ell}{A} = \frac{(20)\ (0.2)}{(0.57)} = 7 \text{ ohms} .$$

Further experiments are planned to fully exploit this technique of investigation of oxidation kinetics.

DISCUSSION

The data in Figures 18, 21 and 22 show rather strikingly that electrochemistry plays a significant role in the stress corrosion cracking of Ti:8-1-1. A preliminary theory is developed here, based for the most part on electrochemical observations. Some parts of the theory are believed to be on a sound footing and other parts are still speculative at this time. It is hoped that it will serve as a basis for further experiments that will lead to a more quantitative theory by an iterative process. The problem of constructing a theory on SCC of titanium at this time is one of drawing conclusions about what is occurring on a microscopic scale from macroscopic observations and from established electrochemical theory

The configuration of a crack in the metal specimens used in the analysis in the following sections is given in Fig. 30. An included angle of approximately 3 degrees was estimated by eye on the surface of a number of specimens. For lack of more precise measurements it will be assumed that this angle is constant down to the apex. It is planned to make more accurate measurements of the crack geometry because this is an important parameter in the theory.

Three electrochemical reactions that can occur in a propagating crack will be used as a basis for analysis:

$$Ti + 2H_2O \rightarrow TiO_2 + 4H^+ + 4e \qquad \text{Reaction 1}$$

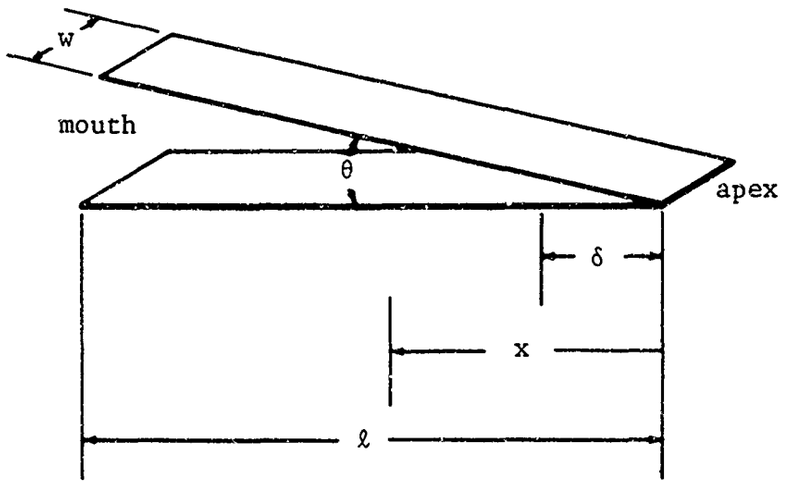

w = thickness of metal specimen (0.127 cm)

ℓ = length of crack

x = distance from apex

δ = length of apex zone with less than one monolayer of oxide

θ = included angle of crack, radians (estimated by eye as approximately 3° for specimen configuration in Fig. 3)

Fig. 30 Configuration of crack in metal used in the analysis.

$$H^+ + e \rightarrow H \qquad \text{Reaction 2}$$

$$Ti + xX^- \rightarrow TiX_x + xe \qquad \text{Reaction 3}$$

Only reactions with titanium are considered here as it is the major constituent in the alloy. The chemistry of other constituents may be delineated when other alloys in addition to Ti:8-1-1 are investigated.

Reaction 1 is the formation of an oxide film on the newly exposed titanium surface on the walls of a propagating crack. Reaction 2 is the reduction of hydrogen ions to hydrogen atoms. The hydrogen, if formed, may go into the metal or evolve as gas. Reaction 3 is the reaction of halide ions, X^-, with titanium to form a halide. In that stress corrosion cracking was very specific to chloride bromide and iodide, it is assumed that reaction 3 occurs at the apex and is responsible in some way for the crack propagation. The reaction may produce either a surface halide or a halide which dissolves in the electrolyte. Dissolution may be followed by hydrolysis as described later.

In the following sections some limiting cases for the electrochemistry in a propagating crack will be examined. A rigorous analysis of current flow into a propagating crack involves consideration of the complex distributed resistance network consisting of the variable electrolyte resistance into the wedge shaped crack and a non-linear oxide film resistance. Two factors contribute to the non-linear electrolyte resistance; the geometry of the crack, and the

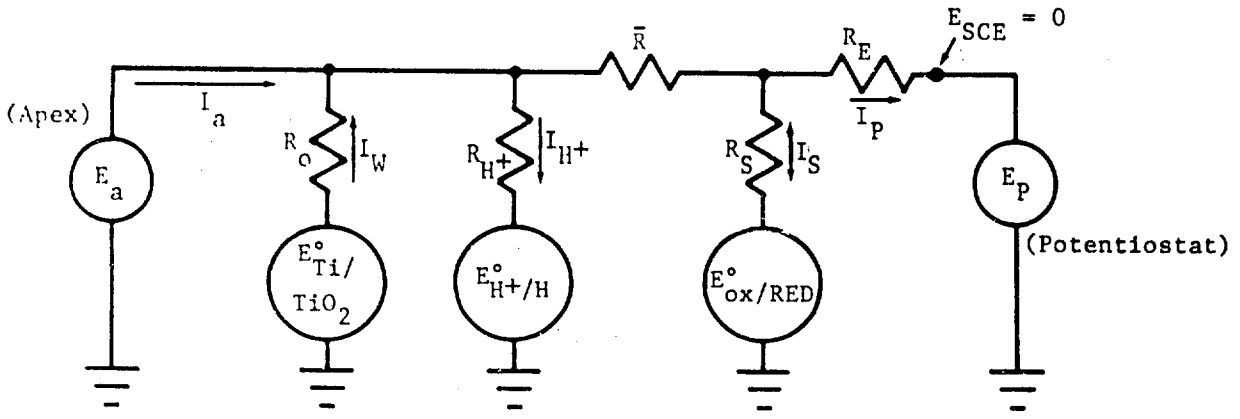

Ground signifies the specimen metal phase.

E_a = Potential at apex.

E_P = Potential applied by potentiostat.

E°_{Ti/TiO_2} = Reversible potential for Ti oxidation (Reaction 1).

$E^\circ_{H^+/H}$ = Reversible potential for H^+ ion reduction (Reaction 2) $E^\circ_{H^+/H} - E^\circ_{Ti/TiO_2} = 860$ mv (Table II).

$E^\circ_{ox/RED}$ = Reversible potential for redox reaction on surface of specimen.

E_{SCE} = Saturated calomel electrode reference potential.

$\bar{R}$ = Average resistance of electrolyte in crack to zone where Ti oxidation occurs at high rate.

R_E = Electrolyte resistance external to crack to tip of Luggin capillary ($R_E \ll \bar{R}$).

R_o = Effective resistance of oxide film and film forming reaction.

R_{H^+} = Effective resistance equivalent to hydrogen overpotential.

R_S = Effective resistance equivalent to the surface redox reaction overpotential.

I_a = Current from apex.

I_W = Current from wall reaction, oxidation of titanium (Reaction 1).

I_{H^+} = Current to hydrogen ion reduction (Reaction 2).

I_S = Current to or from exterior surface reaction.

I_P = Current to potentiostat.

CRITERION FOR SCC INITIATION: $E_a \geq -900$ mv

CRITERIA FOR SCC VELOCITY CONTROL:

1. Potentiostatic control: $R_E \ll R_S$, $\bar{R} \ll R_{H^+}$
2. Surface reaction control: $\bar{R} \ll R_{H^+}$, $I_P = 0$
3. Control by hydrogen ion reduction in crack: $\bar{R} \gg R_{H^+}$

Fig. 31 Equivalent circuit for the electrochemistry in a propagating stress corrosion crack.

and in solutions of different pH will provide data to calculate the hydrogen ion reduction current. The theory will be revised at that time if necessary.

Fig. 31 also gives criteria for SCC velocity control, to be explained in the following sections. Potentiostatic control was used in all of the experiments reported herein.

A. Wall Reactions in the Propagating Crack

The kinetic experiments and the crack velocity determinations provide a key to understanding the events in a propagating crack. The wall reaction will be considered in two parts: (1) a distance δ, near the apex of the crack with less than one monolayer of oxide coverage, and (2) the remaining distance to the mouth of the crack with more than a monolayer of oxide. The distance, δ, will be called the "apex zone". It is believed to be important because, within this zone, halide ions have access to bare titanium metal. The electrochemistry will be different in the apex zone than on the oxide covered metal.

The current flowing to the two walls in the apex zone to form a monolayer of oxide is:

$$I_{aw} = 2wVQ \text{ amp} \qquad \text{Equation 1}$$

The coulombic charge density of a monolayer of oxide, Q, is calculated in Appendix C. This gives an apex wall current of 1.1 μamp at a crack propagation velocity of 1×10^{-2} cm/sec on a 0.127 cm thick

specimen. The corresponding initial measured current (Figures 21 and 22) is about 25 μamp. The difference between the measured current and the apex zone current is assumed to go to the remaining wall out to the mouth of the crack. Additional corrections should be made for the chloride reaction at the apex (described later), current to multiple crack fronts, and the surface oxide healing current (Figure 15) which further reduce the current to the walls. These will be neglected for the present because they are unknown.

The current flowing to the two walls where the oxide is more than a monolayer in thickness is:

$$I_w = 2w \int_{x=\delta}^{x=\ell} i \, dx \quad \text{amps} \qquad \text{Equation 2}$$

The current density for oxide growth based on Fig. 29 can be described approximately by the following expression at a potential of zero mv to SCE:

$$i = \frac{8.8 \times 10^{-4}}{\tau} \quad \text{amp/cm}^2 \qquad \text{Equation 3}$$

For the present analysis this approximate equation will be assumed sufficiently accurate. A more rigorous analysis of the kinetics is given in Appendix D. Potential varies with position x in the crack and would affect the kinetic expression and complicate the analysis but the limiting case of a constant potential will be presented here. The "age" of the surface at a point x distance from the apex is:

$$\tau\ (x) = \frac{x}{V} \text{ sec} \qquad \text{Equation 4}$$

Eliminating i and τ from Equations 2, 3 and 4 and solving gives:

$$I_w = 2(8.8 \times 10^{-4})\ wV \ln \frac{\ell}{\delta} \text{ amps} \qquad \text{Equation 5}$$

This equation can be used to estimate the value of δ, as the other terms can be obtained from experiment. Assuming, for example, that I_w = 23.9 μamp from the difference of the total current and apex zone current, and that just after initiation, ℓ = 0.1 cm, gives $\delta = 2 \times 10^{-6}$ cm. The true value of δ is probably larger than this because I_w is less than 23.9 μamp as stated above.

The rate of film growth is:

$$\frac{dt}{d\tau} = Ai \quad \text{cm/sec} \qquad \text{Equation 6}$$

combining with Equations 3 and 4, eliminating i and τ, and solving for t gives:

$$t = (8.8 \times 10^{-4})\ A \ln \frac{x}{\delta} + t_o \quad \text{cm} \qquad \text{Equation 7}$$

where t_o is thickness of a monolayer of oxide. The value of t_o is assumed to be the diameter of an oxide ion, 2.80 A° from Pauling, 1948.

The calculated oxide thickness is compared to the estimated crack width in Fig. 32 for two values of δ. The value of 2×10^{-6} cm, calculated from the oxidation kinetics, is probably too small as stated above. The value of 2×10^{-4} cm, calculated from the electrolyte

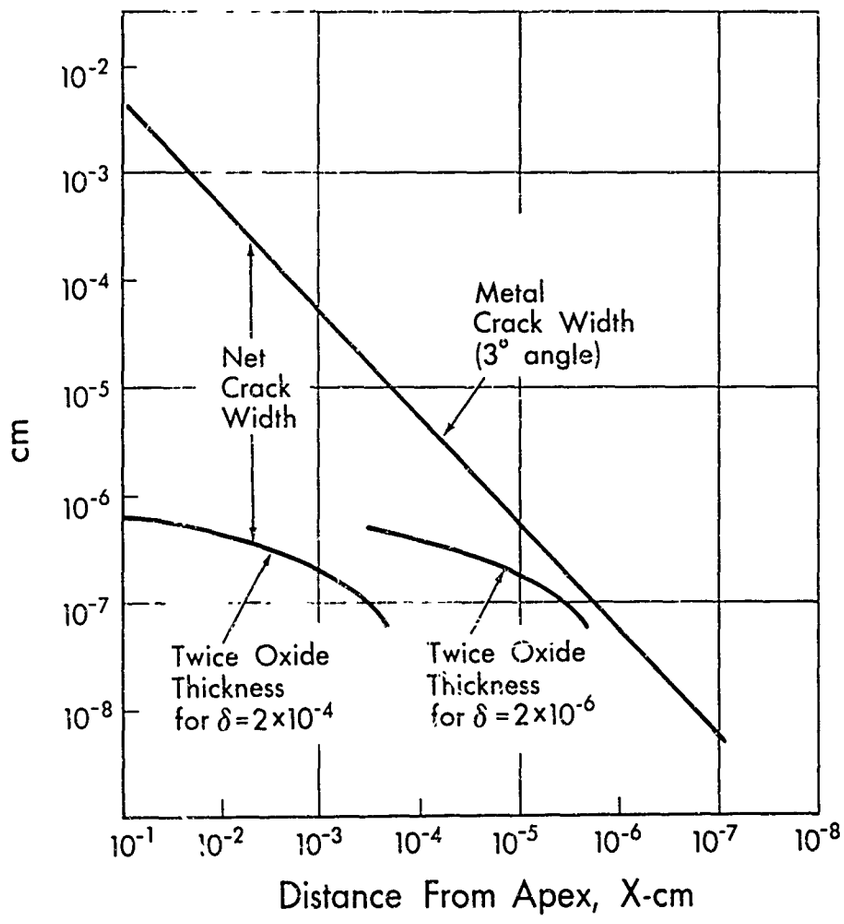

Fig. 32 Estimated crack width and oxide thickness versus distance from apex.

resistance in the next section may be closer to the true value. The difference between the estimated crack width for a 3 degree angle and twice the oxide thickness is the net crack width as shown in Fig. 32. The net crack width would actually be larger than that shown because metal phase is removed to form oxide. The calculated net gain in thickness of metal plus oxide is about 43 percent of the oxide thickness shown.

The existence of a net crack width larger than atomic dimensions would exclude the oxide wedging mechanism. Tentatively, it would appear that the oxide wedging mechanism can be excluded but further investigation of the crack geometry and results from the computer analysis of the current distribution problem will be required in order to make a more definitive answer. The oxide growth and cracking mechanism appears highly unlikely, however, for the experiments on Ti:8-1-1 alloy.

B. Resistance of Electrolyte in Crack

The resistance of the electrolyte from the mouth of a small angle wedge shaped crack to a point x distance from the apex assuming constant electrolyte resistivity can readily be shown to be:

$$R_e = \frac{\rho_e}{w\theta} \ln \frac{\ell}{x} \quad \text{ohm} \qquad \text{Equation 8}$$

This equation can be used to make a second, independent, estimate of the value of δ.

Because the anodizing current falls off very rapidly with time or distance from first monolayer coverage, it can be considered that all of the current flows through a lumped resistance $\bar{R}$ to a narrow zone at a distance the order of magnitude δ from the apex. The resistance calculated from the slope of initial average current in Fig. 22 (roughly corresponding to a crack length of 0.1 cm) is 1.8×10^4 ohms. The resistivity of 0.6 M alkali halide solutions is about 20 ohm cm. A specimen thickness of 0.127 cm and a 3° crack angle therefore gives a distance of about 2×10^{-4} cm for δ. There are several compensating errors in this analysis:

1. all of the current does not flow through all of the resistance,
2. all of the current does not flow into the crack, and
3. generation of hydrogen ion increases electrolyte conductivity thus lowering its resistance toward the apex.

Because of the compensating errors, it cannot be predicted at this time whether the true value of δ is larger or smaller than 2×10^{-4} cm.

C. Mass Transport in the Propagating Crack

In a crack propagating at a constant velocity, the ionic mass transport processes in the electrolyte will be at a quasi steady state in respect to the apex of the crack as point of reference. If halide ion is not incorporated into the metal or oxide or lost by other means there will be no net transport of it. Likewise, if the positive metal ion is not reacted there will be no net transport of it. The only ion

that would then carry current through the electrolyte is the hydrogen ion from reaction 1, occurring at the walls. (In alkaline solutions hydroxyl ions would carry the current.) The fluxes for the three ions may be written (Levich, 1962):

$$J_- = -D_- \nabla C_- + \frac{F}{RT} D_- C_- \nabla\phi = 0 \qquad \text{Equation 9}$$

$$J_+ = -D_+ \nabla C_+ - \frac{F}{RT} z_+ D_+ C_+ \nabla\phi = 0 \qquad \text{Equation 10}$$

$$J_{H^+} = -D_{H^+} \nabla C_{H^+} - \frac{F}{RT} D_{H^+} C_{H^+} \nabla\phi \qquad \text{Equation 11}$$

At steady state, the diffusion flux (first term on the right) is equal and opposite to the migration lfux (second term on right) for halide and metal ions. For the hydrogen ion, the diffusion flux and the migration flux are additive.

If the net flux of halide ion is zero its concentration gradient can be derived from Equation 9.

$$c_1/c_2 = \exp\left(\frac{F}{RT} \Delta\phi_{1-2}\right) \qquad \text{Equation 12}$$

For a $\Delta\phi$ of 0.5 volts (specimen @ -400 mv) in chloride solution, the predicted concentration ratio from apex to bulk electrolyte is 2.8×10^8. This is impossibly high, starting with a bulk concentration of 0.6 molar. Some chloride must therefore go out of solution in the crack either by reaction with metal or oxide or by precipitating out, and thus allow some net flux and a lower concentration ratio. The high chloride concentration ratio, however, explains why dilute bulk chloride solutions (Fig. 23) are still effective in causing stress corrosion cracking.

The increase in halide ion concentration toward the apex is accompanied by an increase in hydrogen ion concentration and a decrease in metal ion concentration. Because of the increased hydrogen halide concentration the conductivity of electrolyte in the crack will be higher than that in the bulk. This factor tends to make the value of δ smaller than calculated in Section B. The increase in hydrogen ion may also cause the solution to go acid enough for hydrogen ion reduction at an apex potential of -900 mv, even though the bulk solution outside of the crack may be alkaline. It is expected that the more rigorous analysis and computer program which considers all of the kinetics and transport phenomena together will give a better approximation to apex conditions.

D. Reactions in Apex Zone

In that stress corrosion cracking was found to occur only in chloride, bromide and iodide solutions it will be assumed that a halide reaction as illustrated by reaction 3 occurs at the apex. The question of whether hydrogen ion discharge (Reaction 2) plays a part in the mechanism is still unresolved. It will be assumed for the moment that it does not and it is hoped that the more rigorous computer analysis and further kinetic experiments will resolve this question.

In order that the attack be preferential to the apex metal atoms they must have a different potential through a higher free energy or a difference in composition such as by short range order. Other-

wise, uniform attack or preferential attack away from the apex and blunting would occur as illustrated in Fig. 33. The magnitude of the increment of potential required depends on the kinetics of the corrosion reaction.

Assume the ratio of the apex corrosion current density, i_a, to the apex zone corrosion current density, i_δ, is $\frac{i_a}{i_\delta} = P$. For the low overpotential case ($\eta < 20$ mv),

$$i = i_o \frac{n\eta F}{RT} , \qquad \text{Equation 13}$$

and $\frac{\eta a}{\eta_\delta} = P$. For the high overpotential case ($\eta > 50$ mv)

$$i = i_o \exp \frac{\alpha n \eta F}{RT} , \qquad \text{Equation 14}$$

and $\eta_a - \eta_\delta = \frac{2.3RT}{\alpha n F} \log P$. (For derivations and explanations of Equations 13 and 14 see for example Potter, 1961. For many reactions $\frac{2.3\ RT}{\alpha n F} = 0.12$ volt or 120 mv.) In the low overpotential case (high exchange current density) only a small difference in free energy between the apex and the apex zone walls may be required for preferential attack of the apex atoms. In the high overpotential case the difference in potential would be about 120 mv per decade of P. An estimation of the increase in free energy of the apex atoms is given in section E.

The flux of halide ions required for cleavage at the apex at a crack propagation velocity V cm/sec can be estimated as follows. Consider a specimen of unit thickness with a row of halide ions at the apex. The number of halide ions in this row is 1/2r ions/cm row, where r is the ionic radius. The number of rows marching in per second

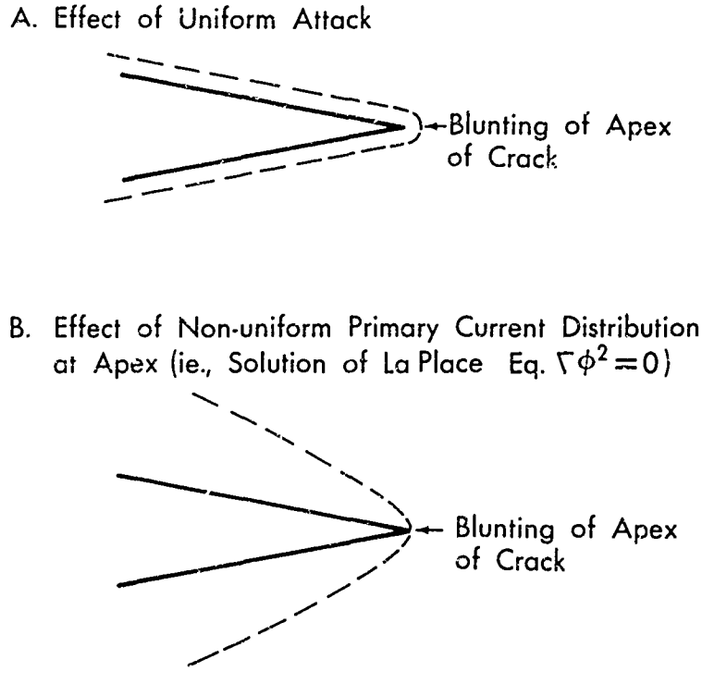

Fig. 33 Electrochemical corrosion of apex of crack.

is V/2r rows/sec (assuming a square array). The current is therefore

$$I_{x^-} = \frac{V\ F}{4\ r^2\ N_A} \quad \text{amps/cm} , \qquad \text{Equation 15}$$

where N_A is Avogadro's number. For a velocity of 10^{-2} cm/sec and a chloride ionic radius of 1.81 A° , $I_{Cl^-} = 1.22 \times 10^{-6}$ amp/cm. For a specimen thickness of 0.127 cm, the apex current is 0.15 μamp. This is small compared to the current for formation of oxide and can be neglected in the total current in the crack. Furthermore, if chloride is not irreversibly reacted, there is an equal and opposite chloride current at approximately δ distance from the apex as chloride is displaced by oxide.

It can readily be shown that in the absence of migration the required concentration difference across the apex zone to bring halide to the apex is:

$$\Delta C_- = \frac{I_{x^-}}{F\ D_-\ \theta}\ \ln\ \frac{\delta}{\delta_a} \qquad \text{Equation 16}$$

Assuming $I_{Cl^-} = 1.22 \times 10^{-6}$ amp/cm, $D_- = 1 \times 10^{-5}$ cm^2/sec, θ = 0.05 (3°) , $\delta = 10^{-4}$ cm, and δ_a 2×10^{-8} cm as closest possible approach of chloride gives $\Delta C_{Cl^-} = 0.22$ mole/liter. With the large concentration increase toward the apex zone from the bulk, there appears to be no problem in chloride transport to the apex in the apex zone.

It is now pertinent to examine what determines the intercept of -900 mv in Figs. 21 and 22. Three possible interpretations are suggested:

1. Reversible potential for formation of titanium oxide or a soluble titanium ion at the acid condition of the apex,
2. Reversible potential for titanium/titanium halide reaction,
3. Point of zero charge for bare titanium metal.

The third is believed to be the most probable at this time.

Standard reversible potentials for some titanium reactions in acid solution are listed in Table IV. Excluding the halide reactions, only formation of TiO_2 (E°_{SCE} = -1100) or TiO^{++} (E°_{SCE} = -1120) give a potential near -900 mv. Addition of a Flade potential for growth of oxide on the surface of an oxide film could account for the difference of about 200 mv. (For explanation of Flade potential, see Vetter, 1961 or Young, 1961). A Flade potential of this magnitude is consistent with values observed for iron and nickel (Vetter, 1961). This interpretation, however, does not throw any light on how the halide ions operate to cause SCC.

The standard reversible potentials for formation of titanium halides, with the exception of the titanium hexafluoride ion, are near the observed -900 mv. It is conceivable that formation of some surface halide complexes could occur at the observed potential. There should be some differences between the values for the three halides but this may be within the error of the extrapolation.

At potentials more positive than the point of zero charge of a metal, anions are adsorbed to the exclusion of water molecules

	$E^{o}_{(SCE)}$ -mv
$Ti + 2H_2O \rightarrow TiO_2 + 4H^+ + 4e$	-1100
$Ti \rightarrow Ti^{+2} + 2e$	-1870
$Ti \rightarrow Ti^{+3} + 3e$	-1450
$Ti + H_2O \rightarrow TiO^{++} + 2H^+ + 4e$	-1120
$Ti + 6F^- \rightarrow TiF_6^{=} + 4e$	-1430
$Ti + 2Cl^- \rightarrow TiCl_2 + 2e$	- 960
$Ti + 3Cl^- \rightarrow TiCl_3 + 3e$	-1020
$Ti + 4Cl^- \rightarrow TiCl_4 + 4e$	- 630
$Ti + 2Br^- \rightarrow TiBr_2 + 2e$	-1160
$Ti + 3Br^- \rightarrow TiBr_3 + 3e$	- 980
$Ti + 4Br^- \rightarrow TiBr_4 + 4e$	- 760
$Ti + 2I^- \rightarrow TiI_2 + 2e$	-1040
$Ti + 3I^- \rightarrow TiI_3 + 3e$	- 810
$Ti + 4I^- \rightarrow TiI_4 + 4e$	- 810

Table IV Standard Reversible Potentials for Some Titanium Reactions (Based on Latimer, 1952)

(Appendix E). Halide ions could therefore exclude water molecules from the apex of a crack in titanium. The specific halide reactions then begin at a potential near the point of zero charge. It is suggested that this is the most probable interpretation of the -900 mv intercept in Figs. 21 and 22.

It is desirable to check the reasonableness of a potential of -900 mv as the point of zero change of titanium. Although there is no known experimental determination, it can be estimated by the approximate linear relation between point of zero change and work function for metals, Frumkin 1965. Such a correlation shown in Appendix E gives -650 ± 400 mv versus SCE for titanium, in reasonable agreement with the proposed -900 mv.

E. Stress and Free Energy of Apex Metal Atoms

It can be shown that the free energy increase of a metal by elastic deformation is

$$\Delta\phi_{\sigma} = \frac{(\frac{1}{2} \times 10^{-7})M\sigma^2}{Y \rho z F} \text{ volts.} \qquad \text{Equation 17}$$

Using the physical properties of titanium tabulated in Appendix A, the free energy increase from zero stress to the yield point is about 0.4 mv, assuming a one electron electrochemical process to then occur. (The rate determining step of metal oxidation is most probably a one electron process.) This increment of free energy appears to be too small to appreciably influence the kinetics of reaction even for the low over-potential case. It will be assumed that a higher level

of elastic stress is required at the apex titanium atoms in order to cause selective anodic reaction of halide.

The maximum free energy increase would correspond to the theoretical strength of the titanium. Assuming the theoretical strength to be Y/10 (Gilman, 1962), the maximum free energy change $\Delta\phi_\sigma$ = 60 mv. This is large enough to influence the kinetics for the low overpotential case.

Another method of estimating the ultimate-strength free energy change is by means of surface energy:

$$\Delta\phi_\gamma = \frac{10^{-7}\ M\ \gamma}{t\ \rho z\ F} \quad \text{volts} \qquad \text{Equation 18}$$

where t is the effective thickness of metal atoms at the surface in which the surface energy is concentrated. Assuming that t = c/2 distance for titanium, that γ 1500 erg/cm^2 typical of many solid metals, and again a one electron process gives $\Delta\phi_\gamma$ = 700 mv. This is probably an upper limit for the free energy increase.

The question to be answered is: what is the mechanism by which the free energy of the atoms in the vicinity of the apex are raised from the yield point energy to a level approaching the theoretical strength where differences in free energy are large enough to significantly affect electrochemical kinetics? The dislocation pileup theory of Zener, 1948, is one possible mechanism. An alternate mechanism is described below.

A proposed model for the stress concentration at the apex of a crack illustrated in Fig. 34. It is proposed that the decision

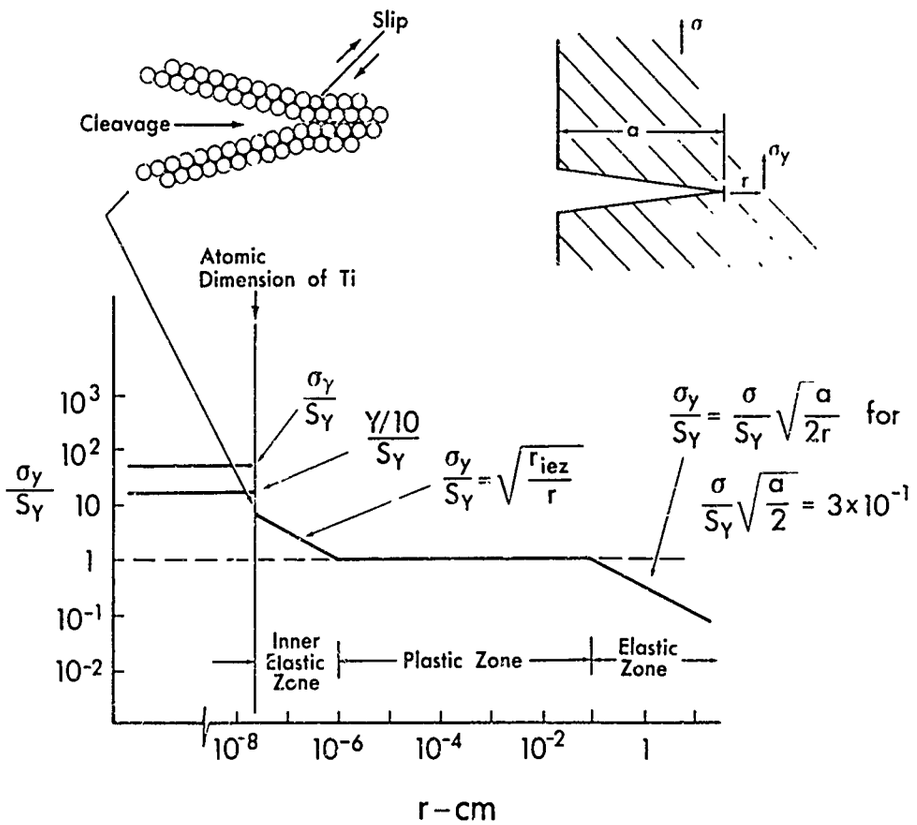

Fig. 34 Proposed model of stress conditions at apex of a metal crack.

as to whether a cleavage crack propagates or whether slip is initiated (thus blunting the crack front) is made on an atomic scale near the crack apex. The modified Griffith treatment using a sharp crack of length a in an isotropic, elastic, infinite plate of unit thickness is the basis. The stress σ_y in the y direction at r distance into the material along the axis of the crack is related to the stress at infinite distance from the crack, σ, by the expression (Paris and Sih, 1965) :

$$\frac{\sigma_y}{\sigma} = \sqrt{\frac{a}{2r}} \qquad \text{Equation 19}$$

In a real material a plastic zone is formed around the apex of the crack beginning at a distance r, where the stress σ_y equals the yield stress of the material, S_Y . Equation 1 is normalized by S_Y and plotted in Fig. 34. This mode of the theory is already established.

If it is now assumed that forces for the initiation are very large compared to forces for movement of mobile dislocations, then the volume between dislocations can be considered as an elastic continuum down to dimensions approaching atomic size. Assuming the same square root relation for the distance r as in Equation 19 and that $\frac{\sigma_y}{S_Y} = 1$ at $r = r_{iez}$ gives for the "inner elastic zone" :

$$\frac{\sigma_y}{S_Y} = \sqrt{\frac{r_{iez}}{r}} \qquad \text{Equation 20}$$

An approximation for the distance between dislocations is $r_{iez} = \rho_d^{-\frac{1}{2}}$.

Equation 20 is plotted in Fig. 34 for a dislocation density of 10^{-12} cm suggested by Blackburn. This gives about a ten fold increase in stress within atomic dimensions of the apex. A ten fold increase in stress gives a one hundred fold increase in potential by Equation 17, or about 40 mv increase in free energy. This would be large enough to significantly influence the kinetics, particularly for the low overpotential case.

It is proposed that an intercept of Equation 20 at atomic dimensions which exceeds the theoretical strength would cause cleavage to occur without specific environmental effects. The higher intercept could be caused by an increase in yield strength or by a decrease in the mobile dislocation density. This might explain the low strength of the notched mill-annealed specimens in air and the lack of sensitivity to chloride solutions as shown in Fig. 27.

The stress conditions for stress corrosion cracking would be when the intercept of Equation 20 at atomic dimensions is above the yield strength but not quite to the theoretical strength. Ions with the right chemical properties can then approach the apex of a crack in the metal and selectively attack the stressed apex metal atoms.

F. Anodic Passivity in Chloride and Bromide Solutions

Figs. 21 and 22 indicate that the mechanism for SCC in chloride, bromide and iodide solutions is the same. Fig. 21 further indicates no substantial shift in the apex potential with applied potential or with crack propagation velocity. This suggests no substantial increase

in the current density for reaction 1 near the apex when anodic passivity occurs in chloride and bromide solutions, because reaction 1 is proceeding at high overpotential. Anodic passivation in chloride and bromide solutions then appears to be due to a limitation in rate of reaction 3 at the apex, or possibly blunting of the apex as in Fig. 33 by a general increase in reaction 3 as the potential increases slightly.

Shutting off reaction 3 could be explained by the chloride and bromide not reaching the apex. One possible mechanism is that the chloride and bromide could be incorporated into the oxide on the crack walls on the way to the apex. This mechanism is consistent with the size of the halide ions given in Table V. Fluoride ion is about the same size as the oxide ion and could easily be incorporated into the oxide at all potentials where the oxide forms. Thus fluoride ion would never reach the apex zone and could not cause stress corrosion cracking. This is consistent with the kinetic data in Fig. 29. Chloride and bromide ions being somewhat larger, would not fit as well into the oxide lattice and would require a higher potential to be driven in. Iodide ion, which is still larger might not be forced into the oxide at the potentials studied and would not be consumed by a wall reaction. Therefore no anodic passivation would occur in iodide solution. Incorporation of chloride and bromide but not iodide at a potential of zero volts to SCE, however, is not consistent with the kinetic data in Fig. 29.

Ion	Radius - A°
$O^{=}$	1.40
F^{-}	1.36
Cl^{-}	1.81
Br^{-}	1.95
I^{-}	2.16

Table V Crystal Radii of Oxide and Halide Ions (Pauling, 1948)

Another mechanism to explain loss of chloride and bromide from the apex zone is the formation of a soluble covalently-bonded neutrally-charged tetrahalide which can diffuse out of the apex zone without migration to bring it back. This is consistent with the observation of a flocculent white precipitate in solution under pitting corrosion conditions in chloride and bromide solutions. The soluble tetrahalide formed during the pitting corrosion process apparently diffuses away from the metal surface and hydrolyzes to TiO_2 in the bulk electrolyte. This mechanism in a propagating crack could carry the halides out of the apex zone. A higher rate of hydrolysis of the relatively weakly bonded titanium tetraiodide could account for no observed flocculent precipitate in iodide solution at high positive potential. The hydrolysis occurring close enough to the surface would deposit oxide in and around the forming pits. A high hydrolysis rate could similarly give regeneration of iodide within the apex zone and thus no net loss of iodide from it. In the case of fluoride a very stable hexafluoride complex ion is formed, at -1430 mv, which would effectively remove fluoride ion from the apex zone.

The passivity observed under all potentials in sulfate, nitrite, perchlorate, and sulfide ion solutions can be attributed to their incorporation into the oxide on the walls. All other oxyanions would be expected to behave in the same way. Hydroxyl ion will react with titanium to give TiO_2 as does water.

G. High Anodic Potential SCC in Halide Solutions

The further loss in strength at high anodic potentials in chloride, bromide and iodide solutions (Fig. 18) could be explained by halide ion discharge on the oxide covered walls. The neutral halide molecules would not be driven into the oxide by its potential gradient. The neutral halide molecules thus formed could then diffuse into the apex zone and be reduced to halide ions on the bare metal. The halide ions could then cause SCC by the mechanism already described. The data in Table VI show that the threshold potential for "anodic" SCC is more positive than the reversible potentials for the halides, which is consistent with this mechanism.

An alternate hypothesis is that the threshold for "anodic" SCC is related to pitting corrosion as suggested by Table VI. Initiation of pitting could produce a multitude of stress risers that allow SCC to proceed again. Initiation of SCC with metal specimens with 20 mil root radius notches at +1000 mv in 0.6 M bromide and iodide solutions as shown in Fig. 17 could be by this mechanism. Electropolishing of the notches perhaps removed nucleation sites and thus prevented this type of SCC initiation in 0.6 M iodide solution.

A somewhat more speculative mechanism is that surface diffusion of halide ions on the oxide above its point of zero charge at which pitting initiates might possibly again bring halide ions to the apex zone. The work of Kolotyrkin, 1963 points to pitting corrosion initiating at the point of zero charge of the oxide.

	Potential - mv vs SCE			
	Standard Reversible Potential		Measured Pitting Potential	Threshold For Anodic SCC (3)
	Latimer, 1952	Measured(1)		
F^-/F_2	+2630	-	-	-
Cl^-/Cl_2	+1120	+1050	<+2000(4)	<+2000
Br^-/Br_2	+ 820	+ 800(2)	+900 to 1000(2)	<+1000
I^-/I_2	+ 300	+ 300	-	+ 700

Notes:

1. Measured in polarization cell on commercially pure titanium - see Fig. 1.
2. See Fig. 10.
3. See Fig. 18.
4. Observed in SCC test.

Table VI. Threshold for "Anodic" Stress Corrosion Cracking Compared to Reversible Potential for Halides

H. Threshold Potential for Initiation of SCC in Halide Solutions

The order of chloride, bromide and iodide in respect to the threshold potential for initiation of SCC on the cathodic side in Fig. 18 requires explanation.

There appears to be no consistent trend of the threshold potential with the reversible potentials given for the halide ions in Table IV. Therefore the threshold potential for initiation of SCC does not appear to be due to the onset of a particular electrochemical reaction. The threshold potential in Fig. 18 is in the reverse order from the usual order of affinity for adsorption of halide ions on metal surfaces. Further, the intercept in Fig. 21, believed to be the apex potential, appears to be approximately equal for chloride, bromide and iodide. Therefore, the threshold potentials probably do not represent the points of zero charge for the halide ions. The diffusivities of chloride, bromide and iodide ions in aqueous solutions are nearly equal, so that differences in the mass transport rate in the electrolyte also cannot explain it.

One hypothesis offered is that the order of the threshold on the cathodic side is due to a steric effect. Iodide ion is larger than the chloride and bromide as shown in Table V, and a higher surface pressure may be required to force it into the small angle apex. Higher surface pressure could be developed by a higher potential acting on the apex zone because of the potential gradient in the electrolyte in the apex zone.

A second related hypothesis involves surface diffusion. As the crack narrows to atomic dimensions near the apex, surface diffusion may be required to transport the halide ions to the apex titanium atoms. A higher adsorption affinity of the iodide ions may impede the surface diffusion. A higher surface pressure gradient may therefore be required to get adequate rates of surface diffusion.

The curve for iodide in Fig. 18 also shows a "shoulder" between -500 mv and -700 mv that is as yet unexplained. One possibility is that this is due to trace amounts of chloride and bromide. The analysis on the reagent bottle indicated less than 0.01% total chloride and bromide reported as chloride. Further work to resolve this question is planned.

I. Effect of Concentration

The apparent constancy of potential at which susceptibility begins on the negative potential side in hydrochloric acid solutions as shown in Fig. 23 is consistent with either the point of zero charge hypothesis or chloride ion discharge. The shift in potential for anodic protection at low HCl concentrations could be attributed to the high resistivity of the solution and loss of control of the crack propagation rate by the potentiostat ($\bar{R} >> R_H$ in Fig. 31). The HCl concentration would increase toward the apex and reaction 2 occurring on the walls could satisfy the current for reaction 1 on the walls. Plots of the limited data on average crack propagation velocity from

those experiments in the dilute solutions where the potentiostat apparently had control, indicated a -900 mv intercept and a smaller dV/dE slope in lower concentration as expected from a larger electrolyte resistance.

The disappearance of SCC at low chloride concentration in 0.6 molar KOH solution as shown in Fig. 24 may be attributed to lack of chloride ions at the apex. The hydroxyl ions at a higher concentration and mobility would be the predominant negative charge carriers in solution. The disappearance of SCC with addition of hydroxyl ion to iodide solution as shown in Fig. 25 could be attributed to the same cause. The same explanation would apply to the mixtures of 0.6 M NaCl and NaF solutions as shown in Fig. 26.

J. Prediction of Crack Propagation Velocity under Open-Circuit Conditions

All of the SCC experiments described in this report were done under potentiostatic conditions. In this section a method for predicting the crack propagation veloctiy under open circuit conditions is outlined. This is the surface reaction control criterion on Fig. 31. The method remains to be verified experimentally.

Crack propagation velocity from Fig. 21 and average initial current from Fig. 22 are replotted in Fig. 35. In order to get a straight line on a logarithmic plot, the difference between the applied potential and the intercept potential of -900 mv in Fig. 21 was used as abscissa.

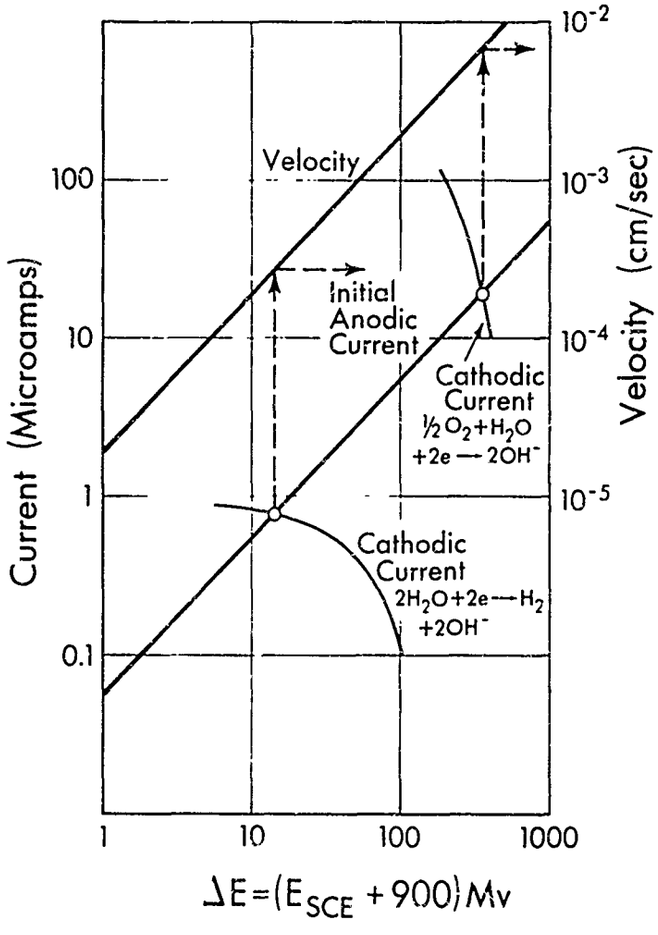

Fig. 35 Estimation of stress corrosion cracking velocity under open-circuit conditions.

Under open circuit conditions the anodic current required for crack propagation must come from an equal cathodic current elsewhere on the specimen. It was assumed that the cathodic current could come from the approximately 10 square cm of exterior surface of the specimen exposed to electrolyte solution in the cell of Fig. 4. Two reactions were considered; generation of hydrogen and reduction of dissolved oxygen. For purpose of illustration, the polarization curves from Fig. 8 were replotted in Fig. 35. The intersection of the anodic and cathodic current curves gives the "operating point." Projection of this current to the velocity curve would give the propagation velocity under these conditions.

Many more variables would affect the crack propagation velocity under open circuit conditions. These include: contact area of electrolyte to the exterior surface, conductivity of the electrolyte, concentration of reducible species, composition of the metal, overpotential for reduction, surface conditions of the metal, and other metals in contact with the specimen and electrolyte. This would account for much of the scatter in the usual stress corrosion cracking data.

K. Summary of Mechanism

A qualitative summary of the variables and relationships believed to be operative in stress corrosion cracking of Ti:8-1-1 alloy is shown in Fig. 36. Various limiting cases of the oxidation kinetics and mass transport problem were examined in this report. These provided some further insights into the mechanism and pointed out areas

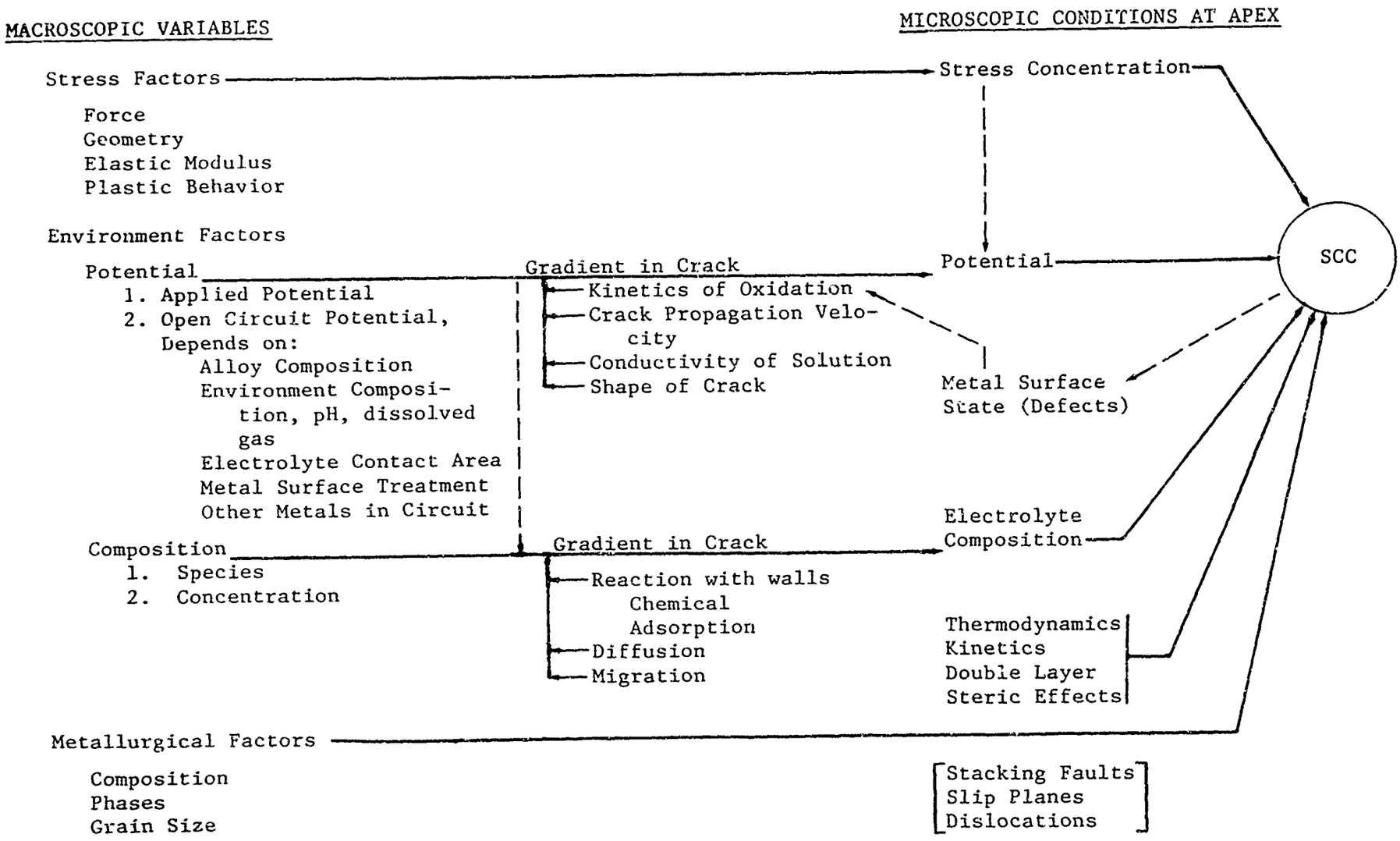

Fig. 36 Summary of stress corrosion cracking variables and mechanisms.

where further experimental work should be done. Some additional metallurgical factors not dealt with in this report are added to Fig. 36 for completeness. Fractographic analyses and work with other alloys is expected to throw some light on these factors.

In summary, the following comments may be made in respect to the proposed mechanisms described in the Introduction.

1. Hydrogen mechanism. It is still not resolved from this work whether formation of hydride plays any role in SCC of titanium. It is not necessary to the proposed mechanism but it has not been disproven. Reduction of hydrogen ions is possible if the solution becomes acid at the apex of the propagating crack. The composition of the solution at the apex of a propagating crack remains to be determined. If the hydrogen mechanism is involved, however, it is only in conjunction with chloride, bromide and iodide.

2. Oxide mechanism. An oxide mechanism operating by wedging or by brittle fracture appears unlikely based on the interpretation of the oxidation kinetics data. The oxide film growth, however, does appear to play a role in limiting the crack propagation velocity.

3. Anodic dissolution. The anodic attack of the higher energy metal atoms at the apex by chloride, bromide and iodide appears to be the preferred mechanism at this time.

4. Adsorption mechanism. Adsorption of halide ions at potentials more positive than the point of zero charge is believed to initiate SCC. It may be difficult to distinguish between anodic

attack and adsorption on an atomic scale if the product of reaction remains on the metal surface.

CONCLUSIONS

The following conclusions are based on experiments with duplex annealed Ti:8-1-1 alloy specimens in aqueous solutions at room temperature:

1. SCC is specific to Cl^-, Br^- and I^- ions and to date no others, e.g., F^-, OH^-, $S^=$, $SO_4^=$, NO_2^-, ClO_4^-.
2. Cathodic protection occurs at a potential more negative than -900mv to SCE.
3. At applied potentials more positive than -900mv to SCE, the velocity of crack propagation is controlled by electrochemistry, i.e., $V = K (E + 900)$ for Cl^-, Br^- and I^- solutions.
4. A region of anodic protection occurs for Cl^- and Br^-, but not for I^- solutions.
5. SCC occurs in Cl^-, Br^-, and I^- solutions at high anodic potentials.
6. An electrochemical mechanism has been developed that predicts the velocity relationship, semiquantitatively with existing data. Qualitatively, the model can explain the anodic passivity and loss of passivity at higher anodic potential.
7. The model provides a basis for further definitive experiments.

FUTURE WORK

The following items of work are planned as a continuation of this investigation:

1. Test other Ti alloys and heat treatments. Develop understanding of mechanisms in the metal phase.
2. Determine metal thickness effect. Delineate the contribution of stress and electrochemical effects.
3. Make fractographic analyses of fracture surfaces and correlate with SCC conditions.
4. Determine crack geometry more accurately.
5. Determine by radiographic techniques the relation of halide ion absorption in forming TiO_2 to potential.
6. Determine the kinetics of hydrolysis of titanium halides.
7. Continue and refine the high speed oxidation kinetics studies on Ti at less than monolayer oxide coverage. Determine kinetics of hydrogen ion discharge
8. Continue the computer analysis of the electrochemical kinetics and mass transport in developing crack. Use new kinetic parameters as developed.
9. Put all experimental data on punched cards and make computer data reduction and correlations.

ACKNOWLEDGMENT

The author is indebted to Dr. M. J. Blackburn for considerable help in designing and conducting the experiments and for many hours of fruitful discussion of mechanisms, Prof. E. A. Grens of Berkeley for helping in the development of the ideas on the mass transport phenomena, and Prof. E. Orowan and Dr. A. W. Smith, and all others of the staff at BSRL who listened patiently to the somewhat nebulous ideas as they were developing and made constructive criticisms. A special note of thanks goes to Mr. Paul Olson who contributed his skill to designing and building the cells and fixtures used in this program, and to Mrs. H. Wallner who conscientiously conducted most of the tensile tests and kept the records in order.

REFERENCES

American Institute of Physics Handbook, McGraw-Hill, New York, 1963

T. N. Andersen, R. S. Perkin, and H. Eyring, J. Am. Chem. Soc., 86, 4496 (1964)

L. I. Antropov, "Kinetics of Electrode Processes and Null Points of Metals", Council of Scientific & Industrial Research, New Delhi, 1960

T. R. Beck and M. J. Blackburn, Research Proposal, D1-82-0467, August 1965

B. F. Brown, ASTM Annual Meeting, June 13-18, 1965

A. N. Frumkin, Soviet Electrochemistry, 1, 341 (1965)

J. J. Gilman, "Strength of Ceramic Crystals", Am. Cer. Soc. Conf., New York, 1962

T. Hurlin, Acta Chemica Scandinavica, 13, 365 (1959)

H. A. Johanson, G. B. Adams, and P. Van Rysselberghe, J. Electrochem. Soc., 104, 339 (1957)

G. C. Kiefer and W. W. Harple, Metal Progress, p. 74, Feb. (1953)

Ja. M. Kolötyrkin, Corrosion, 19, 261t (1963)

W. Latimer, "Oxidation Potentials", 2nd Ed., Prentice-Hall, Englewood Cliffs, N. J., 1952

V. Levich, "Physico Chemico Hydrodynamics" (Translation), Prentice-Hall, Englewood Cliffs, N. J., 1962

National Bureau of Standards, "Handbook of Mathematical Functions with Formulas, Graphs, and Mathematical Tables", Ed. - M. Abramowitz and I. A. Stegun, pp. 245-248 (1964)

P. C. Paris and G. C. Sih, in "Fracture Toughness Testing and its Applications", Special Technical Publication 381, ASTM, 1965

L. Pauling, "The Nature of the Chemical Bond", Cornell University Press, Ithica, N. Y., 1948

E. C. Potter, "Electrochemistry", Cleaver-Hume Press Ltd., London, 1961

M. Stern and H. Wissenberg, J. Electrochem. Soc., 106, 759 (1959)

K. Vetter, "Electrochemische Kinetik", Springer-Verlag, Berlin, 1961

L. Young, "Anodic Oxide Films", Academic Press, New York 1961

C. Zener, Trans. ASM, A40, 3 (1948)

APPENDIX A

NOMENCLATURE

A = constant $\frac{M_o}{zF\rho}$ cm^3/coulomb

= area, cm

a = jump distance in oxide, cm

= crack depth, cm

= lattice parameter

C = concentration, mole/cm^3

c = lattice parameter

D = diffusivity, cm^2/sec

E = potential, volts

E° = standard reversible potential, volts

F = Faraday, 96,500 coulomb/equiv or 23,060 cal/volt equiv

I = dimensionless current density i/i_o

I = current, amps

i = current density, amp/cm

i_o = exchange current density

i_c = corrosion current density

ℓ = length, cm

ln = logarithm base e

log = logarithm base 10

M = molecular weight, gm/mole

N_A = Avogadro's number, 6.02×10^{23} atom/mole

n = number of electrons in rate determining step

P = ratio of current density

Q = charge density of monolayer, coul/cm^2

R = gas constant, 1.987 cal/deg mole

R_e = resistance, ohms

$\overline{R}$ = lumped resistance, ohms

r = distance from crack apex in the metal, cm

= ionic radius, cm

S_Y = yield strength of metal, dyne/cm^2

t = thickness of oxide or surface metal layer, cm

U = ultimate force, Kg

V = crack propagation velocity, cm/sec

w = thickness of specimen, cm

x = length, cm

Y = Youngs modulus, dyne/cm^2

z = equiv/mole

α = transmission coefficient, dimensionless

β = constant $\frac{\alpha z F a}{RT}$, cm/volt

γ = surface energy, dyne-cm/cm^2

δ = length of apex zone, cm

δ_o = closest approach of ion to crack apex, cm

η = overpotential volts

θ = angle, radians

ρ = density, gm/cm^3

ρ_d = dislocation density, cm/cm^3

ρ_e = resistivity, ohm cm

σ = stress, dyne/cm^2

τ = time, sec

T = $\tau / \left(\frac{\beta \Delta \phi}{Ai_o}\right)$ dimensionless time parameter

ϕ = potential, volts

Subscripts

A = Air

A = Avagadro's number

a = apex

aw = apex wall

c = corrosion

d = dislocation

E = external

e = electrical resistivity

F = Flade potential

H^+ = hydrogen ion

iez = inner elastic zone

m = mobile

o = exchange current

= oxide reaction

= monolayer of oxide

p = potentiostat

s = salt

S = surface

SCE = saturated calomel electrode

SHE = standard hydrogen electrode

w = wall

we = working electrode

wf = work function

X^- = halide ion

y = y direction

Y = yield strength

$-$ = anion

$+$ = cation

APPENDIX B

Physical Properties of Titanium

Atomic weight, $M = 47.90$ gm/mole

Density, $\rho = 4.50$ gm/cm^3

Youngs modulus, $Y = 11.0 \times 10^{11}$ dyne/cm^2 $(16.0 \times 10^6$ psi)

Lattice parameters,

$a = 2.950$ A^o

$c = 4.683$ A^o

Yield strength of duplex annealed Ti:8-1-1

$Sy \approx 9.0 \times 10^9$ dyne/cm^2 (130,000 psi)

APPENDIX C

Charge Density of a Close Packed Monolayer of Oxide Ions

Bases: (1) Adsorption of oxide ions on basal plane of titanium.

(2) Assume one double charged oxide ion per surface titanium atom.

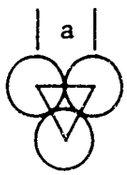

Area of triangle = $\frac{\sqrt{3}}{4} a^2$.

Contains 3 x 1/6 = 1/2 atom of Ti.

$A = \frac{\sqrt{3}}{2} a^2$ cm^2/atom

$$Q = \frac{2F}{A N_A} = \frac{2.31 F}{a^2 N_A} \text{ coul/cm}^2 \qquad \text{Equation 21}$$

For $a = 2.95 \times 10^{-8}$ cm (Appendix B),

$Q = 425 \times 10^{-6}$ coul/cm^2.

APPENDIX D

Growth Rate of Anodic Oxide Film on Titanium

The growth rate of an anodic oxide film starting from a molecular thickness is (for example, Vetter, 1961, p. 621):

$$\frac{dt}{d\tau} = A(i-i_c) \qquad \text{Equation 22}$$

$$i = i_o \exp\left(\frac{\beta\Delta\phi}{t}\right) \qquad \text{Equation 23}$$

A solution of these equations may be obtained for a plane electrode under potentiostatic conditions ($\Delta\phi$ = constant). From equation 23,

$$t = \frac{\beta\Delta\phi}{\ln(i/i_o)} = \frac{\beta\Delta\phi}{\ln I}$$

and

$$dt = -\frac{\beta\Delta\phi \; d\ln I}{(\ln I)^2}$$

assuming that $i >> i_c$ during the initial period of film growth,

$$d\tau = -\left(\frac{\beta\Delta\phi}{Ai_o}\right) \frac{d \ln I}{I (\ln I)^2}$$

or

$$dT = \frac{d\tau}{\left(\frac{\beta\Delta\phi}{Ai_o}\right)} = -\frac{dI}{I^2(\ln I)^2} \qquad \text{Equation 24}$$

The solution computed from tabled Exponential Integral E_2 (Handbook of Math. Funct., NBS, 1964) is plotted in Fig. 37. Values for the constants are:

$$\beta_{Theor} = \frac{\alpha z F a}{RT} = 2.3 \times 10^{-6} \quad \text{cm/volt}$$

for $\alpha = 0.5$, $z = +4$ for Ti^{+4}, $a = 2.96 \times 10^{-8}$ cm. (c spacing in rutile, Hurlen, 1959), $T = 298.2$ °K

Johansen, et al, 1957, give experimentally measured values for titanium of:

$$\beta_{exp} \approx 5.6 \text{ to } 6.7 \times 10^{-6} \text{ cm/volt}$$

An average experimental value of about 6.0×10^{-6} will be used.

$$A = \frac{M_o}{zF\rho} = 4.85 \times 10^{-5} \text{ cm}^3\text{/coulomb for rutile.}$$

$$i_{o_{exp}} \approx 0.5 \text{ to } 9 \times 10^{-13} \text{ amp/cm}^2 \quad \text{(Johanson et al, 1957).}$$

An average value of 2×10^{-13} will be used.

$$\Delta\phi = E - E_o - E_F - \eta(i) \text{ volts} \qquad \text{(Vetter 1961, p. 621)}$$

where $\eta(i)$ is the overpotential for the surface reaction

$H_2O \rightarrow 2\ H^+ + O^=$ (oxide)

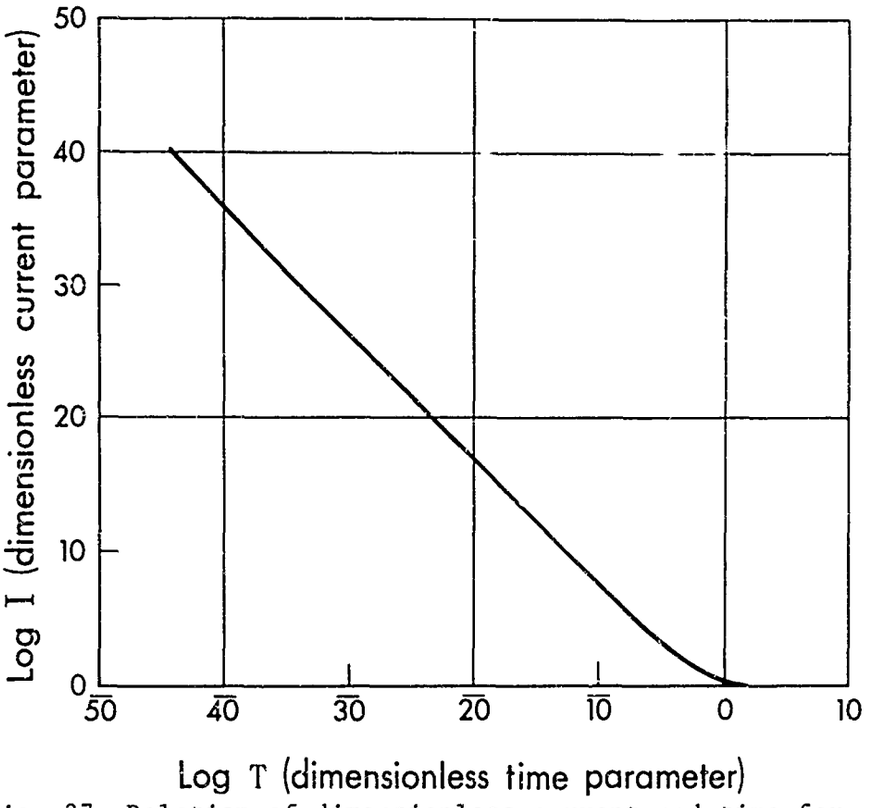

Fig. 37 Relation of dimensionless current and time for potentiostatic growth of anodic oxide film.

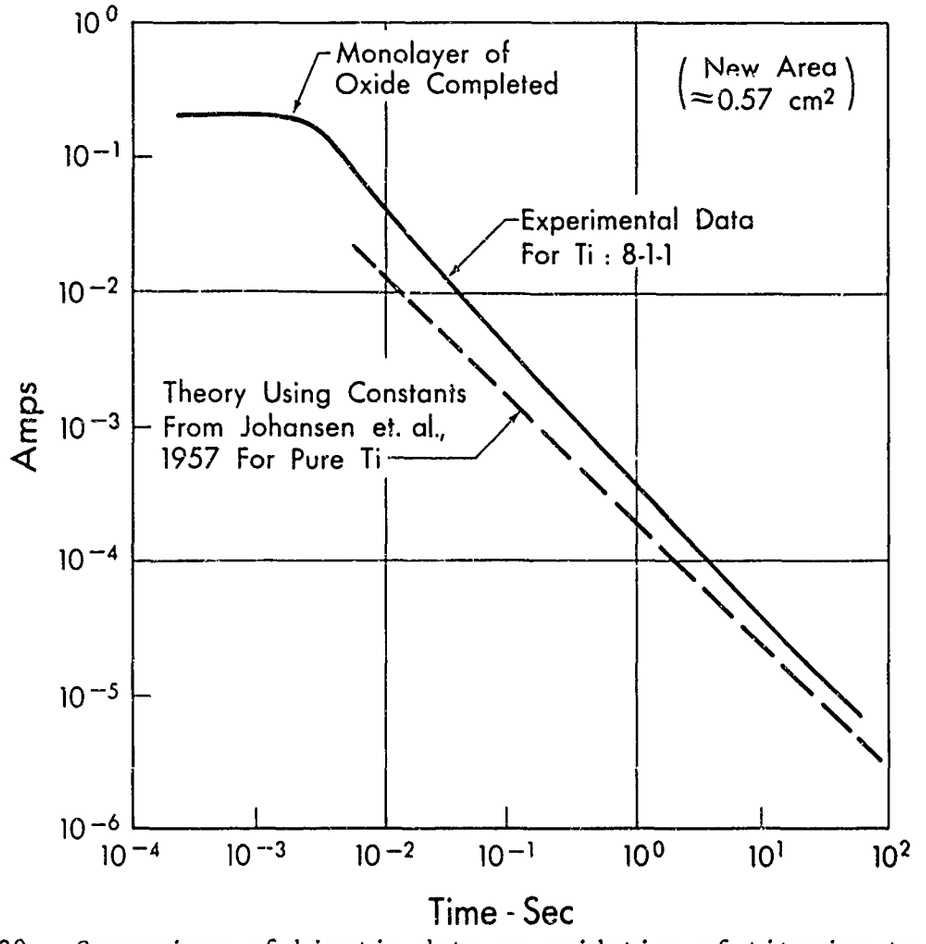

Fig. 38 Comparison of kinetic data on oxidation of titanium to theory using constants from literature.

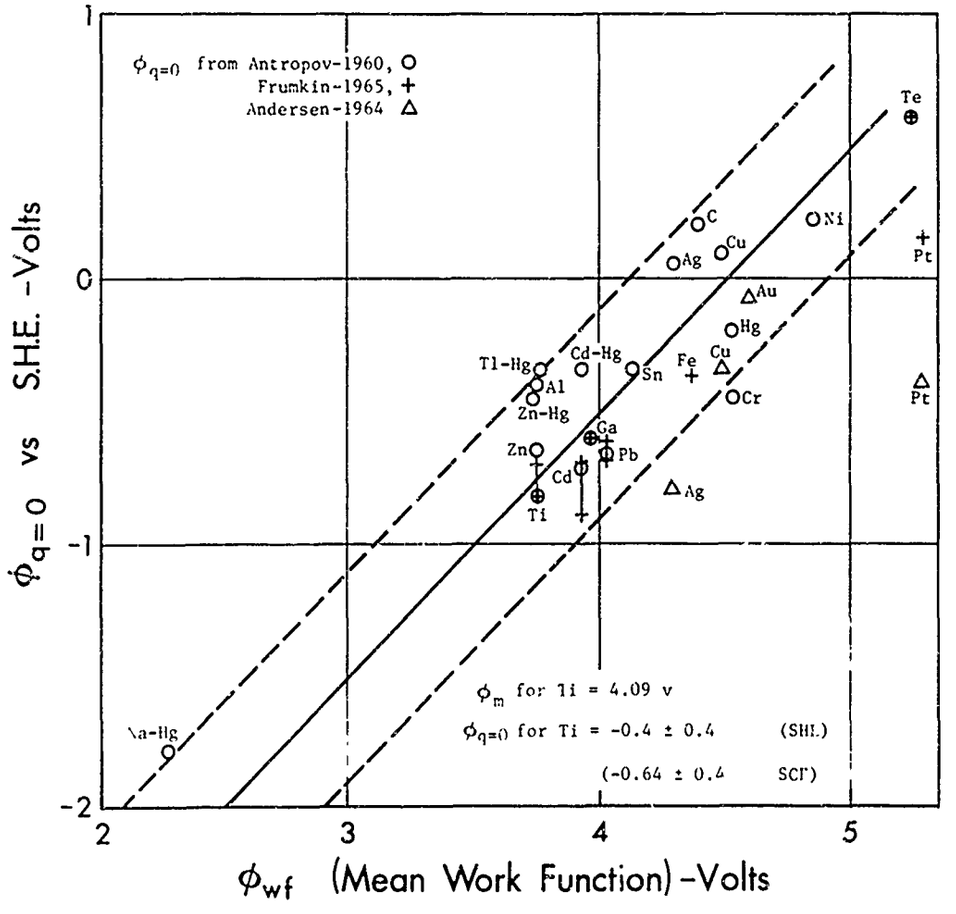

Fig. 39 Estimation of point of zero charge.